Geochemistry Geophysics Geosystems G3
AN ELECTRONIC JOURNAL OF THE EARTH SCIENCES
Published by AGU and the Geochemical Society

Article
Volume 9, Number 12
17 December 2008
Q12020, doi:10.1029/2008GC002152
ISSN: 1525-2027

Crustal thickness variations along the Southeast Indian Ridge (100°–116°E) from 2-D body wave tomography

R. Chadwick Holmes, Maya Tolstoy, James R. Cochran, and Jacqueline S. Floyd

Department of Earth and Environmental Sciences, Lamont-Doherty Earth Observatory, P.O. Box 1000, 61 Route 9W, Palisades, New York 10964, USA (cholmes@ldeo.columbia.edu)

[1] Axial morphology along the Southeast Indian Ridge (SEIR) systematically changes from an axial high to a deep rift valley at a nearly uniform intermediate spreading rate between 100°–116°E, west of the Australian-Antarctic Discordance (AAD). Basalt geochemistry has a consistent Indian–mid-ocean ridge basalt (MORB) type isotopic signature, so changes in axial topography are attributed to variations in both mantle temperature and melt supply. Wide-angle seismic refraction lines were shot to four ocean bottom hydrophones within SEIR segments P1, P2, S1, and T, where each segment is characterized by a different morphology. We constructed 2-D crustal velocity models by jointly inverting hand-picked *P* wave refraction (Pg) and Moho reflection (PmP) traveltime data using a top-down, minimum-structure methodology. The results show a 1.5 km eastward decrease in crustal thickness across the study area, with segment averages ranging from 6.1 km at P1 to 4.6 km at T. Melt generation models require a ~30°C decrease in mantle temperature toward the AAD to account for the crustal thickness trend. Significant changes in axial morphology accompany small-scale variations in crustal thickness, consistent with models of crustal accretion where ridge topography is determined by a balance between mantle temperature, melt supply, and cooling from hydrothermal circulation. Layer 3 thins by 3.0 km as layer 2 thickens by 1.4 km between segments P1 and T, reflecting the eastward decrease in melt supply and increase in melt lens depth. The trade-off in seismic layers may be explained by models relating the increase in overburden pressure on a deepening melt lens to the volume of magma erupted into the upper crust rather than cooling at depth to form new lower crustal material.

Components: 12,003 words, 14 figures, 3 tables.

Keywords: Southeast Indian Ridge; mid-ocean ridge; crustal structure; oceanic crust; seismic tomography; seismic refraction.

Index Terms: 3025 Marine Geology and Geophysics: Marine seismics (0935, 7294); 7220 Seismology: Oceanic crust; 7245 Seismology: Mid-ocean ridges.

Received 2 July 2008; **Revised** 1 October 2008; **Accepted** 27 October 2008; **Published** 17 December 2008.

Holmes, R. C., M. Tolstoy, J. R. Cochran, and J. S. Floyd (2008), Crustal thickness variations along the Southeast Indian Ridge (100°–116°E) from 2-D body wave tomography, *Geochem. Geophys. Geosyst.*, *9*, Q12020, doi:10.1029/2008GC002152.

1. Introduction

[2] The fast- and slow-spreading end-members of the global mid-ocean ridge system represent distinct structural modes defined by a unique set of morphological characteristics. Fast spreading ridges (>90 mm/a full rate) like the East Pacific Rise (EPR) are marked by a prominent axial high,

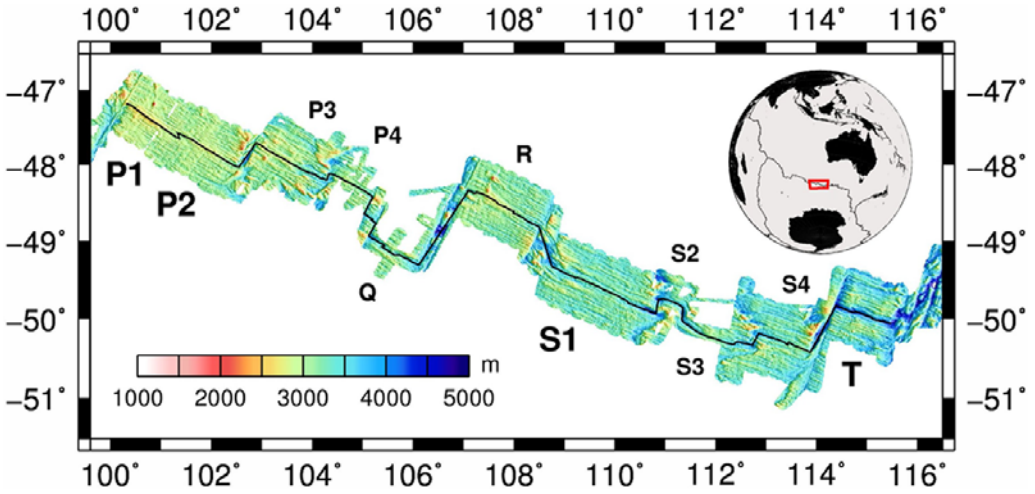

Figure 1. Shaded relief map of multibeam bathymetry for the section of the Southeast Indian Ridge surveyed by cruise EW0114. The solid line marks the ridge axis. Inset shows the location of the study region in a global context. Labels identify first- and second-order ridge segments. Larger labels indicate segments where seismic refraction data were acquired.

smooth ridge flanks, and both seismic and geologic evidence of frequent eruptive activity [*Menard*, 1960; *Macdonald*, 1982, 1989]. By contrast, slow-spreading ridges (<40 mm/a full rate) like the Mid-Atlantic Ridge (MAR) are characterized by a 15–40 km wide, 1–3 km deep axial rift valley and rough, faulted topography [*Heezen*, 1960; *Macdonald*, 1982, 1986]. Although axial depth and relief tend to decrease with increasing spreading rate [*Menard*, 1967; *Macdonald*, 1986; *Small*, 1994], studies do not support a smooth morphological transition between an axial high and an axial valley. *Small and Sandwell* [1989] concluded that a threshold-type mechanism governs axial form based on how abruptly characteristics of Geosat altimetry gravity profiles change at spreading rates of 60–70 mm/a. Global variations in across-axis ridge topography suggest the ridge-valley transition occurs over an interval of only 10–15 mm/a [*Malinverno*, 1993]. Similarly abrupt transitions are also evident in measurements of along-axis gravity roughness [*Small and Sandwell*, 1992], on-axis mantle Bouguer anomaly (MBA) gradients [*Lin and Phipps Morgan*, 1992; *Wang and Cochran*, 1995], and basic morphologic parameters like axial relief, cross-axis profile asymmetry, bathymetric roughness, and zero-age depth [*Small*, 1998].

[3] A full determination of how the transition between fast- and slow-spreading ridge morphologies takes place is a necessary component to understanding the processes behind crustal accretion along mid-ocean ridges. Studies of intermediate spreading ridges can provide the needed insight into how individual tectonic, geochemical, and thermal parameters control ridge-axis structure. The Southeast Indian Ridge (SEIR) west of the Australian Antarctic Discordance (AAD) offers a unique setting where the nearly constant intermediate spreading rate and consistent mid-ocean ridge basalt (MORB)-type isotopic signature isolate axial thermal structure as the controlling factor on ridge topography. In this study, we present our analysis of seismic refraction data collected between 100° and 116°E along four segments of the SEIR that exhibit very different types of axial morphology. We employ *P* wave traveltime tomography to produce 2-D models of velocity structure and crustal thickness within each segment and subsequently discuss the implications for variations in melt supply, mantle temperature, and the systematic evolution of ridge morphology across our study area.

2. Tectonic Setting

[4] The Southeast Indian Ridge (SEIR) forms the boundary between the Australian and Antarctic Plates, extending from the Rodriguez Triple Junction (25°S, 70°E) east of Madagascar to the Macquarie Triple Junction (63°S, 165°E) south of New Zealand. Detailed tectonic reconstructions of the region face continual reassessment due to the paucity and complexity of magnetic data, but evidence shows seafloor spreading initiated near the Great Australian Bight in the Late Cretaceous (likely 96 Ma) [*Cande and Mutter*, 1982; *Veevers*, 1986] and remained ultraslow (1.5–4.5 mm/a half-rate) until the breakup between

the Kerguelen Plateau and Broken Ridge beginning in the early Eocene [*Cande and Mutter*, 1982; *Royer and Sandwell*, 1989; *Tikku and Cande*, 1999]. Subsequent rate increases in the mid-Eocene (chron 18, ~40 Ma) and early Oligocene (chron 13, ~34 Ma) established the intermediate range of rates observed today [*Royer and Sandwell*, 1989], which vary from 69 mm/a full-rate near 88°E to 75 mm/a near 120°E [*DeMets et al.*, 1994].

[5] The Australian-Antarctic Discordance (AAD) is an anomalously deep (>4 km) and pervasively fractured segment of the SEIR between ~120° and 128°E. The regional negative depth anomaly [*Weissel nd Hayes*, 1974; *Hayes*, 1988], negative free-air gravity anomalies [*Weissel and Hayes*, 1974; *Cochran and Talwani*, 1977], high Rayleigh wave velocities [*Forsyth et al.*, 1987; *Kuo et al.*, 1996], and major element basaltic geochemistry [*Klein et al.*, 1991] all suggest the AAD overlies a region of low mantle temperatures. Isotopic studies show the AAD marks an abrupt transition between Indian-MORB and Pacific-MORB-type mantle [*Klein et al.*, 1988; *Pyle et al.*, 1992], consistent with the convergence and downwelling of along-axis asthenospheric flow [*Weissel and Hayes*, 1974; *Hayes*, 1988; *West et al.*, 1997], although the disruption of mantle convection by a remanent subducted slab has also been proffered [*Gurnis et al.*, 1998; *Ritzwoller et al.*, 2003; *Gurnis and Müller*, 2003].

[6] By contrast, the SEIR shallows to 1–2 km depth between 76° and 78°E as it crosses the massive (>30,000 km^2) Amsterdam-St. Paul (ASP) plateau, the product of enhanced crustal accretion fueled by the ASP hot spot over the past ~4 Ma [*Conder et al.*, 2000; *Scheirer et al.*, 2000]. Geophysical observations [*Small*, 1995; *Ma and Cochran*, 1996] and minor isotopic evidence [*Hamelin et al.*, 1986; *Michard et al.*, 1986] suggest material from the distant (~1500 km) Kerguelen-Heard (K-H) hot spot group may also reach the ridge near 84°E, although some are skeptical of this claim [e.g., *Mahoney et al.*, 2002].

3. Study Area

[7] This study examines the tectonic corridor south-southeast of Australia between the 100°E transform fault and the 116°E transform complex (Figure 1), a 1200 km section of ridge spreading at a nearly constant rate of 72 ± 1 mm/a [*DeMets et al.*, 1994]. Although along-axis variations in the Nd-Pb-Sr isotopic signature of basalts exist, samples from this region indicate the melt source is singularly Indian-MORB-type mantle [*Klein et al.*, 1988; *Mahoney et al.*, 2002]. The study area contains six first-order ridge segments lettered P through T by the nomenclature of *Cochran et al.* [1997] (Figure 1), with numbers delineating second-order segmentation due propagating rifts (PR) and overlapping spreading complexes (OSC). Active PRs at 104°15′E, 111°E, and 112°45′E all trend eastward in the direction of a 1500 m increase in axial depth and 500 m increase in ridge flank depth [*Phipps Morgan and Sandwell*, 1994; *Ma and Cochran*, 1997]. Ridge morphology varies across the study area as well, exhibiting four distinct modes as it transitions from an axial high to an axial valley between segments P1 and T. A number of other geophysical and morphological characteristics similarly change between 100°E and 116°E: mean magnetic anomaly amplitudes weaken by 80 nT [*Ma and Cochran*, 1996], mantle Bouguer gravity anomalies (MBA) increase by 50 mGal [*Cochran et al.*, 1997], abyssal hill relief (bathymetric roughness) grows by 50 m [*Ma and Cochran*, 1996, 1997; *Goff et al.*, 1997], and subsidence rates decrease by 40 m/Ma [*Kane and Hayes*, 1994; *Géli et al.*, 2007].

[8] Multichannel seismic (MCS) data collected along segment P1 image a bright reflector at shallow depths (1480 m below seafloor (bsf)) attributed to the presence of an axial melt lens [*Baran et al.*, 2005]. The reflector depth increases to 2100 m bsf in segment P2, then to 2320 m bsf in P3, and is fully absent from segment P4 [*Baran et al.*, 2005] (Figure 1). Variations in seismic layer 2A thickness accompany this trend, increasing from 300 to 450 m between segments P1 and P4 [*Baran et al.*, 2005]. Rapid transitions in axial morphology also take place between segments P1 and P2 and within segment P3 [*Sempéré et al.*, 1997; *Shah and Sempéré*, 1998] (Figures 1 and 2). This covariation of morphology and melt lens depth has similarly been noted in segment R [*Baran et al.*, 2005] as well as along sections of the Galapagos Spreading Center (GSC) [*Blacic et al.*, 2004].

Figure 2. Detailed bathymetry and shot line geometry for segments (a) P1, (b) P2, (c) S1, and (d) T. The bathymetric grid consists of 150-m resolution Seabeam2000 data supplemented by two minute resolution altimetry-derived topography [*Sandwell and Smith*, 1997]. The contour interval is 250 m. Solid black lines mark the individual refraction lines. Stars indicate the drift-corrected positions of the four OBHs deployed along each line.

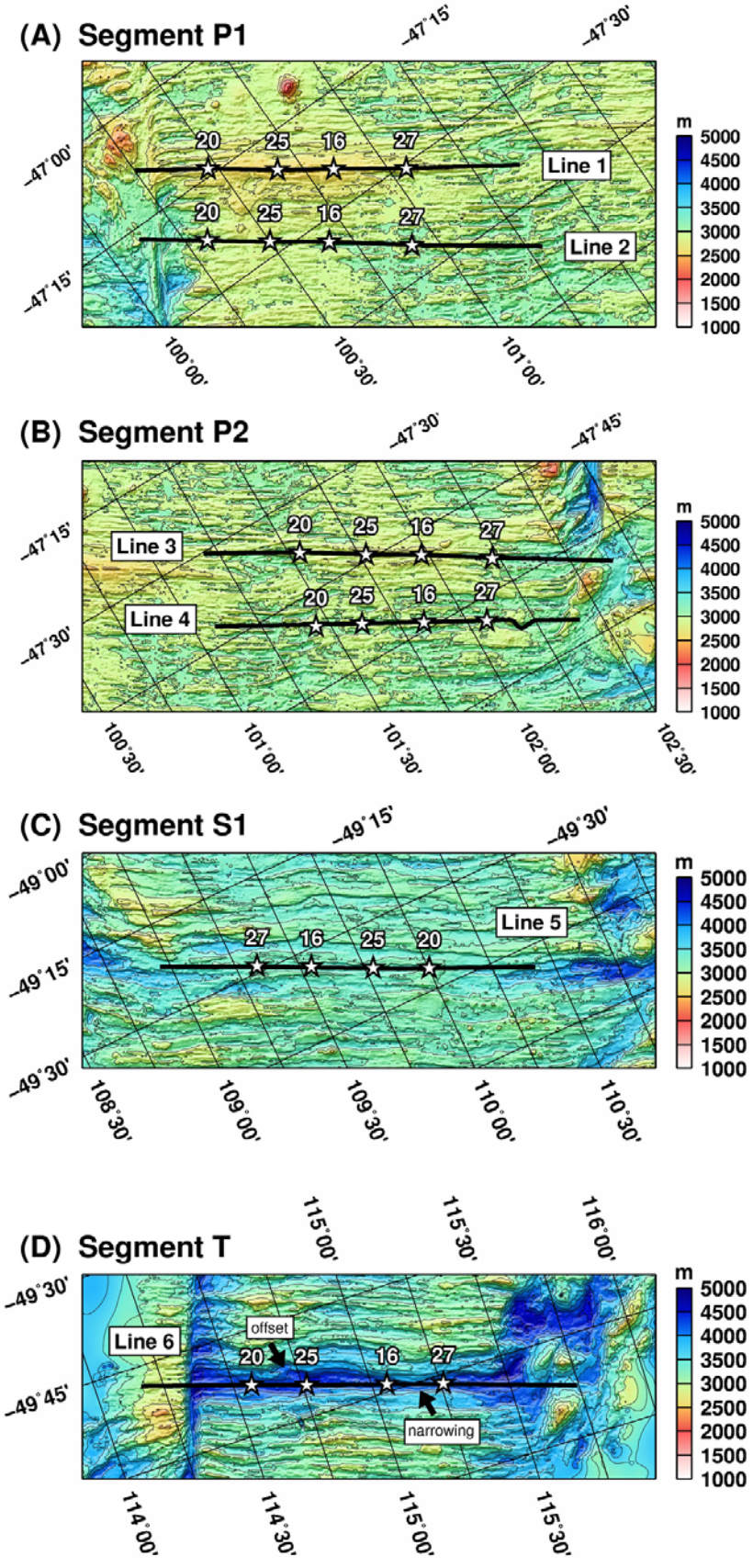
(A) Segment P1
-47°15'
-47°30'
-47°00'
-47°15'
20
25
16
27
Line 1
Line 2
100°00'
100°30'
101°00'
m
5000
4500
4000
3500
3000
2500
2000
1500
1000
(B) Segment P2
-47°30'
-47°45'
-47°15'
-47°30'
Line 3
Line 4
100°30'
101°00'
101°30'
102°00'
102°30'
(C) Segment S1
-49°15'
-49°30'
-49°00'
-49°15'
-49°30'
Line 5
27
16
25
20
108°30'
109°00'
109°30'
110°00'
110°30'
(D) Segment T
115°00'
115°30'
116°00'
-49°30'
-49°45'
Line 6
offset
narrowing
114°00'
114°30'
115°00'
115°30'

Figure 2

[9] We focused on four distinct segments (P1, P2, S1, and T) within our study area to further examine the relationship between ridge morphology and crustal structure. Segment P1 (100°E transform to 101°30′E OSC, Figure 2a) is characterized by a robust axial high that stands ~400 m above the ridge flanks near the segment midpoint [*Shah and Sempéré*, 1998]. M1 and M2 (88°30′–90°30′E) are the only other segments west of the AAD with similarly well-developed EPR-like highs [*Cochran et al.*, 1997]. The SEIR more commonly displays the more subdued "rifted high" morphology of segment P2 (101°30′E OSC to the 102°45′E transform, Figure 2b) distinguished by a central 1–4 km wide, 200 m deep axial graben flanked by small-offset (50–100 m) normal faults [*Cochran et al.*, 1997; *Shah and Sempéré*, 1998]. Further to the west, segment S1 (108°30′E transform complex to 111°E PR, Figure 2c) exhibits a "shallow axial valley" morphology similar to intermediate spreading segments along the Juan de Fuca Ridge and the GSC [*Sinton et al.*, 2003; *Baran et al.*, 2005; *Canales et al.*, 2005]. Unlike the matured, 1.0–1.3 km deep axial valley along segment T (114°E transform to 116°E transform complex, Figure 2d), the central rift valley of S1 generally has less than 500 m of topographic relief [*Cochran et al.*, 1997; *Shah and Sempéré*, 1998].

4. Data Acquisition

[10] Six active-source seismic refraction experiments were conducted along segments P1, P2, S1, and T of the SEIR (Figure 1) as part of R/V *Maurice Ewing* cruise EW0114 (from December 2001 to January 2002). Data were recorded at 200 Hz by four WHOI-OBSIP ocean bottom hydrophones (OBHs) [see *Peal et al.*, 1993] deployed 15–20 km apart along each line. Refraction lines were run both on-axis and 20 km south of the axis (~525 ka isochron) within segments P1 and P2 (Figures 2a and 2b). On-axis lines were completed along segments S1 and T as well (Figures 2c and 2d), but extreme weather conditions precluded off-axis work in these areas. All refraction lines ran east to west (into the wind) to reduce the risk of tangling the air gun tow lines.

[11] The R/V *Maurice Ewing*'s 20-element 8445 in^3 (138 L) air gun array served as the seismic source, firing once every 120 s (~275 m shot spacing at a nominal speed of 4.5 knots) from 8 m depth. Shot locations were determined from known firing times and shipboard Global Positioning System (GPS) fixes, subsequently adjusted for the 55 m offset between the Trimble Tasmon P/Y Code receiver and the center of the air gun array. GPS logging occurred at 10 s intervals, resulting in a position accuracy of ~15 m. Concurrent Krupp Atlas Hydrosweep-DS2 center beam measurements provided along-line water depths accurate to 0.2% the depth or 5–9 m.

5. Data Processing

[12] Seismic data recorded by each OBH were converted to the PASSCAL variant of the SEG-Y file format [*Barry et al.*, 1975] for archival and analysis. Timing corrections applied to the data comprise a static offset and a linear drift term determined by comparing the OBH clocks to GPS (UTC) time before deployment and on recovery. These corrections are certain to within the 5 ms sampling interval of the OBH clocks. The seafloor positions of the OBHs were established by inverting direct water wave traveltimes from both the axis-parallel refraction lines and short (~3.5 km) instrument-centered cross lines. The latter were shot with a single 385 in^3 air gun at a 120 s interval for line 1 and a 60 s interval for lines 2–6. Table 1 lists the corrected OBH positions for all six deployments and the location uncertainty characterized by the final RMS error for the water wave picks.

[13] The data were passed through a bandpass Butterworth filter (5–25 Hz, 24 dB/octave sidelobe decay rate) to reduce ocean wave and waterborne noise prior to the identification of *P* wave arrivals. We manually picked traveltimes for first-arriving crustal refractions (Pg) and high-amplitude secondary arrivals attributed to Moho reflections (PmP). There is a progressive decrease in signal quality (Figure 3) and pick totals (Table 3) for lines run further to the east presumably due to the worsening sea conditions and the eastward increase in axial depth and bathymetric roughness. Uncertainty estimates assigned to Pg picks range from 15 to 150 ms and were chosen as a function of the trace signal-to-noise ratio (SNR) at the time of the arrival [*Zelt and Forsyth*, 1994] (Figure 4). The SNR method does not readily apply to PmP picks because Moho reflections arrive within the coda of a preceding phase. Instead we evaluated each refraction line in turn, selecting from a trial suite the smallest PmP pick error value capable of producing a solution fitting the data to the level

Table 1. Results of Instrument Relocation

Line	OBH	Latitude, °S	Longitude, °E	Instrument Depth, m	RMS Error, ms
1	16	47°24.62′	100°50.31′	2456	9
	20	47°13.99′	100°28.15′	2689	5
	25	47°20.00′	100°40.25′	2489	9
	27	47°30.64′	101°03.29′	2671	8
2	16	47°32.95′	100°40.47′	2931	10
	20	47°22.50′	100°19.11′	2953	6
	25	47°27.93′	100°30.02′	2836	10
	27	47°48.70′	100°54.74′	2933	7
3	16	47°38.21′	101°58.42′	2850	6
	20	47°38.21′	101°46.47′	2901	7
	25	47°44.03′	101°32.47′	2771	6
	27	47°55.11′	102°13.25′	3063	7
4	16	47°58.70′	101°50.53′	2974	7
	20	47°50.26′	101°26.71′	2998	18
	25	47°53.74′	101°36.93′	2941	10
	27	48°03.69′	102°04.46′	2954	7
5	16	49°32.85′	109°32.72′	3332	5
	20	49°41.43′	110°00.17′	3293	10
	25	49°37.45′	109°47.05′	3468	5
	27	49°28.87′	109°20.07′	3322	5
6	16	49°58.86′	115°03.38′	4162	6
	20	49°52.84′	114°34.04′	4367	4
	25	49°55.33′	114°45.94′	4336	4
	27	50°01.28′	115°15.64′	4195	7

of the noise. The selected error estimates range from 20 ms for line 2 to 35 ms for lines 5 and 6.

6. Methodology

[14] We applied the method of *Korenaga et al.* [2000] to jointly invert Pg and PmP traveltimes for two-dimensional (2-D) *P* wave structure and crustal thickness. Each model was parameterized as a dense grid of velocity nodes draped on the along-line bathymetry. Nodes were spaced every 500 m laterally and at a vertical interval increasing from 50 m at the seafloor to ~150 m at the base of the mesh (20 km), resulting in a parameter density of 36,200 nodes/100 km. The Moho was parameterized as a series of depth nodes spaced 1 km apart that collectively define a floating reflector independent of specific velocity contours or mesh geometry. The starting depth assigned to the reflector was determined from a suite of trial inversions (Figure A1) such that the chosen value (circled) resulted in the smallest initial $\chi 2$ misfit for PmP traveltimes.

[15] Velocity models for the refraction lines were constructed from the 1-D forward modeling results for line 2 (T2) and line 5 (T5) [*Tolstoy et al.*, 2002] (Figure 8). Specifically, the line 1 and line 2 starting models were based on the T2 profile, as were the models for lines 3 and 4 under the assumption that crustal velocity structure is first-order continuous across the 101°30′E overlapper (Figures 2a–2b). Starting models for lines 5 and line 6 relied on the TL5 profile. The water column was assigned a constant velocity of 1500 m/s to simplify traveltime calculations. Shotpoint water depths were extracted from 150 m resolution gridded SeaBeam2000 multibeam bathymetry along the L1-minimized great circle path through all shot positions. Known source (shot) and receiver (OBH) locations were projected onto the same great circle path, as were layer 2A thickness estimates derived from multichannel seismic (MCS) data collected along separate but coincident shot lines in segments P1, P2, and S1 [*Baran et al.*, 2005]. Layer 2A was incorporated into the starting models as a homogeneous upper crustal layer assigned the line-specific average 2A velocity determined by MCS data analysis (J. M. Baran, personal communication, 2007).

[16] The forward step of the *Korenaga et al.* [2000] inversion method takes a graph theory approach [e.g., *Dijkstra*, 1959] to searching for the minimum traveltime raypaths connecting each source-receiver combination [*Moser*, 1991, *van Avendonk et al.*, 1998]. Graph methods systematically overestimate path lengths with solutions that zigzag across the underlying nodal framework, so a secondary conjugate gradient ray-bending procedure is used to refine the raypaths, resulting in more accurate traveltimes [*Moser et al.*, 1992]. The inverse step applies the LSQR iterative linear least squares method for sparse matrices [*Paige and Saunders*, 1982] on a system regularized with both damping and weighted smoothness constraints [*van Avendonk et al.*, 1998; *Korenaga et al.*, 2000]. Model perturbations generally decrease in magnitude with each iteration of an inversion, so damping parameters were allowed to freely vary under the condition that velocity and depth perturbations never exceeded 5% and 10%, respectively. Depth-dependent correlation lengths are used to define the dimensions of a Gaussian smoothing operator that regulates model roughness. The horizontal velocity correlation length was linearly increased from 2 km at the seafloor to 25 km at the base of the model, and the vertical velocity correlation length similarly ranged from 50 m to 2.5 km. A constant correlation length of 5 km was applied to the reflector. Table 2 lists line-specific smoothness weighting factors that were selected using an L curve analysis of the trade-off between model roughness and data misfit [see *Phillips and Fehler*, 1991; *van Avendonk et al.*,

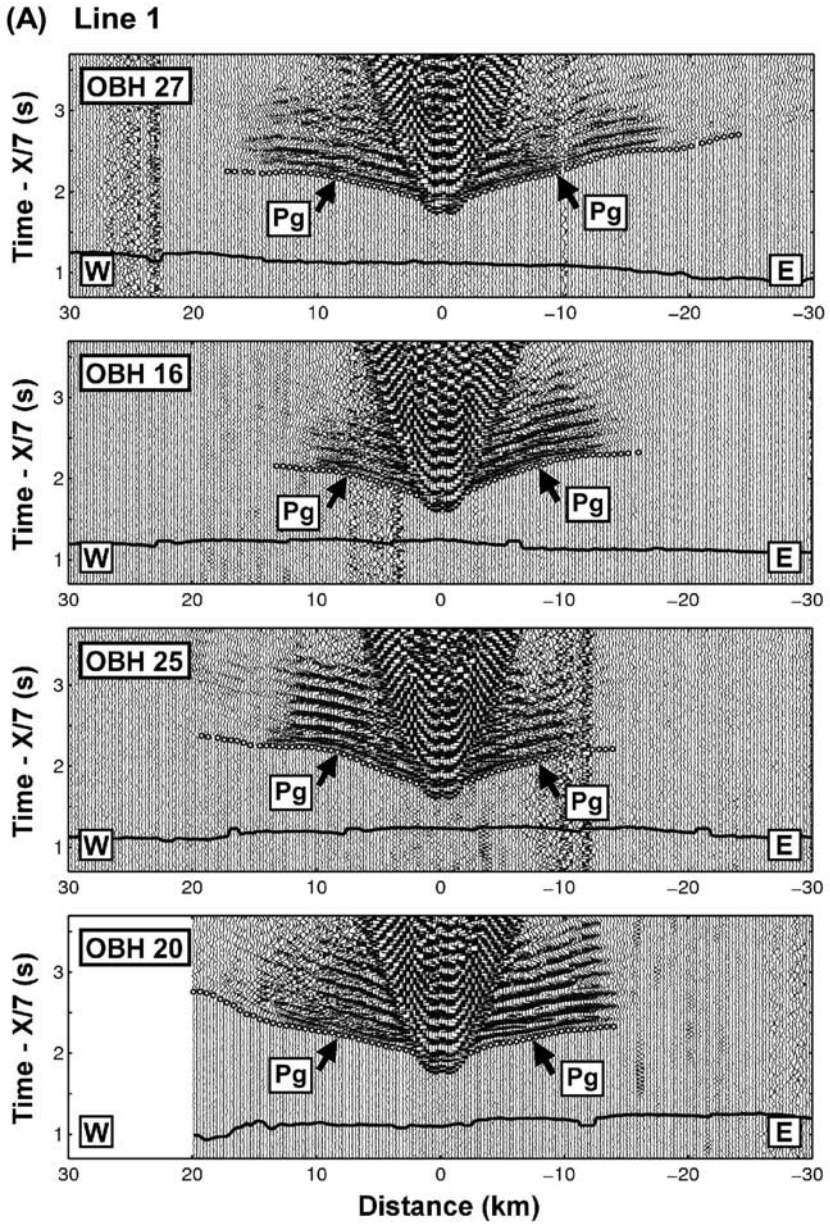

Figure 3. Seismic record sections constructed from OBH data showing (a–f) lines 1 through 6, respectively, with individual instrument records as labeled. The horizontal axis is source-receiver distance. Negative values indicate the ship is east of the OBH. The vertical axis measures traveltime reduced to 7 km/s. Data are bandpass filtered between 5 and 25 Hz. A constant gain is used to preserve true amplitude variations. White circles mark pick locations for the identified phase arrivals. Along-line bathymetry normalized to the fixed range [0,1] is plotted at the bottom of each panel to highlight the influence of topography on the seismic data.

2004]. Also listed is the depth kernel weighting factor (w), a parameter that directly biases the inversion toward fitting PmP traveltime data with perturbations to either velocities in the lower crust or the depth of the reflector. We selected a value of $w = 1.0$ to equally weight both velocity and depth node information and, by consequence, rely on the estimated pick errors to influence where model changes occur. An assessment of model solution sensitivity to this parameter appears in Appendix A.

[17] Tomography solutions were derived using a "layer-stripping" process that focuses first on shallow structure where steep velocity gradients and lateral heterogeneity strongly influence phase arrival times [*Zelt*, 1999; *Rawlinson and Sambridge*, 2003]. By inverting for deeper crustal structure

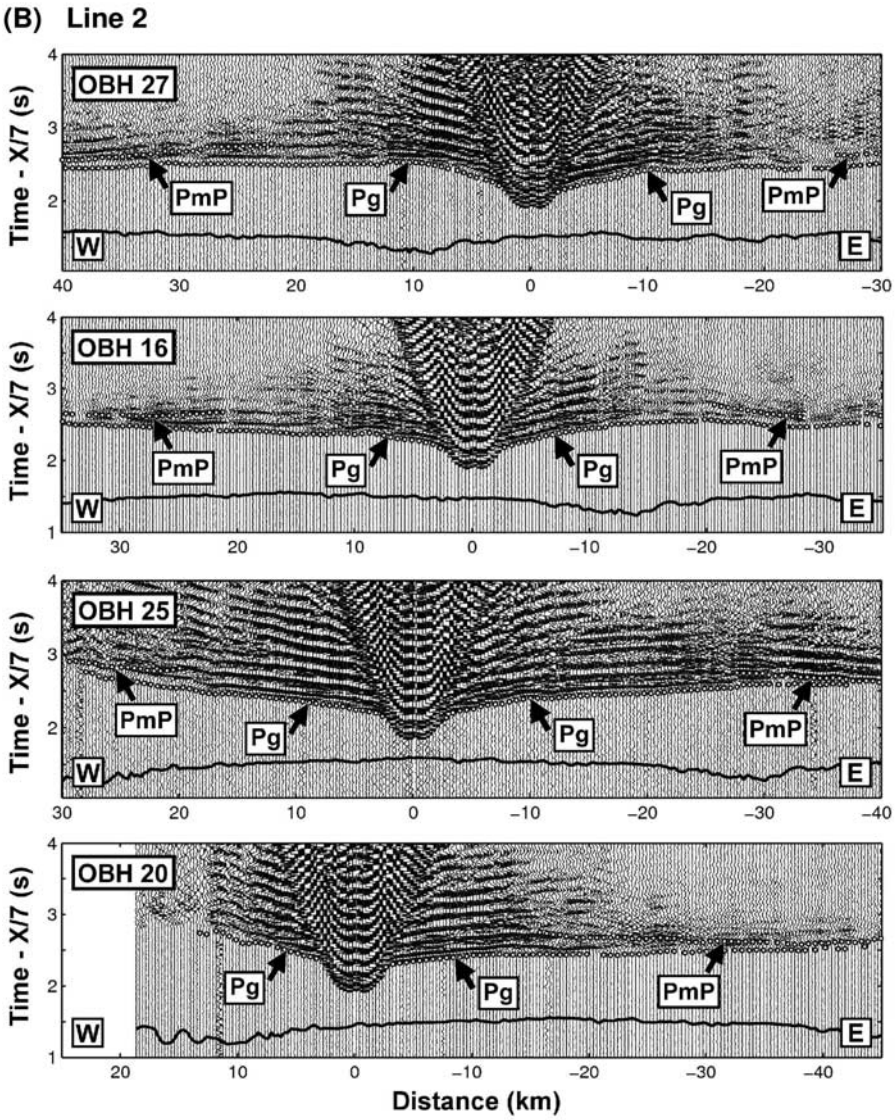

Figure 3. (continued)

from the top down, this method accounts for the systematic decrease in ray coverage with depth, thereby reducing the risk of smearing strong shallow anomalies into the lower crust. Pg traveltime picks were limited to source-receiver ranges of 5 km or less in the first step of the procedure (Figure 5a). The limit was increased to 10 km for the second step, and the third included the full set of refraction data (Figures 5b–5c). The final step iteratively inverted all Pg and PmP data until the solution reached $\chi 2 = 1.0$, our target level of misfit (Figure 5d). We find this process produced models with less lower crustal heterogeneity than other inversion methods, resulting in minimum-structure solutions appropriate for such strongly underdetermined inverse problems [e.g., *Constable et al.*, 1987; *Zelt*, 1999].

[18] Each model solution was divided into crustal units corresponding to seismic layers 2 and 3 in order to investigate variations in velocity structure. The layer 2/3 boundary typically marks a sharp, order of magnitude reduction in velocity gradient (≥ 1 s^{-1} to ~ 0.1–0.2 s^{-1}) at P wave velocities of 6.6 km/s or greater [*White et al.*, 1992]. We adopted more conservative boundary conditions to compensate for the smoothness of model solutions, defining a velocity gradient maximum and P wave velocity minimum of 0.5 s^{-1} and 6.5 km/s, respectively. Layer 2/3 boundary profiles were determined by averaging the results of three different methods in order to out spurious deviations

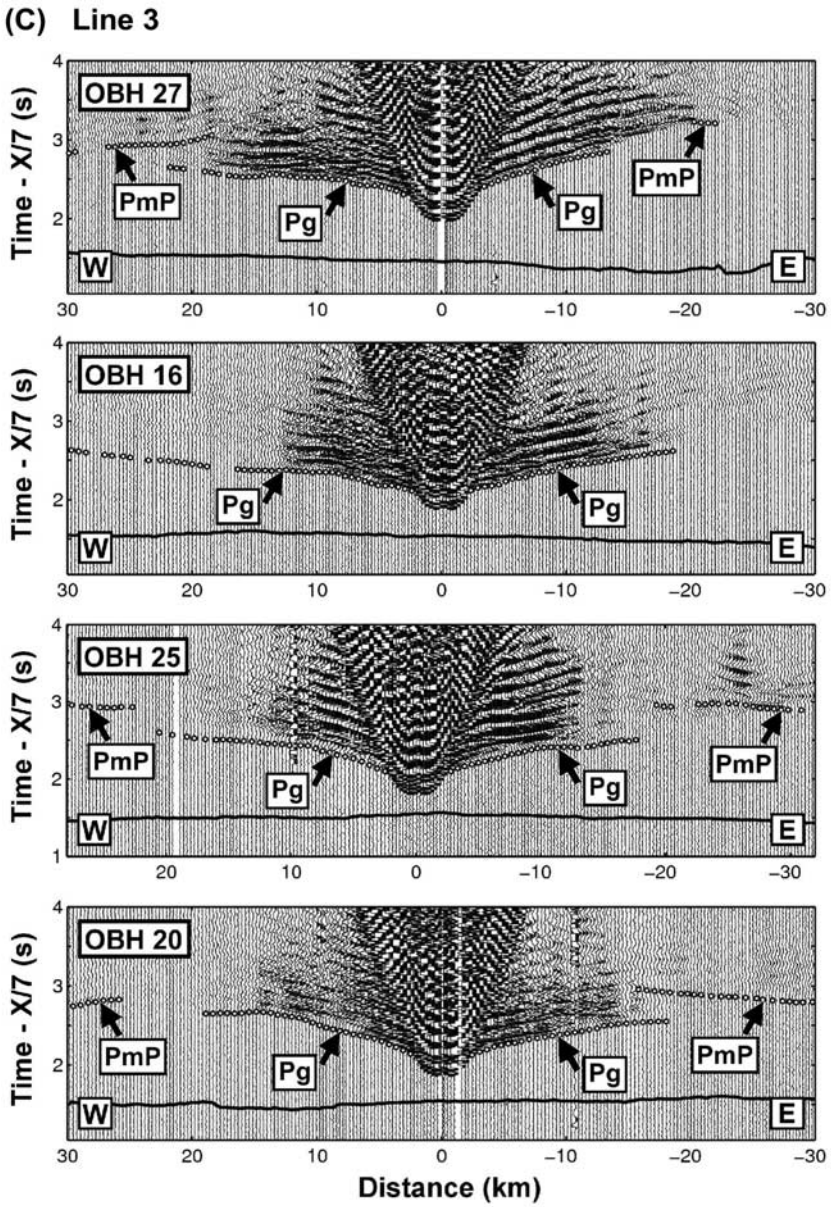

Figure 3. (continued)

that occur within any single solution. The first method identified the depth of the characteristic shift in velocity gradient by locating the uppermost spike in the second derivative of the median 1-D velocity profile (Figure 8) consistent with our boundary conditions. The second method traced the depth contour of the boundary velocity determined by the first method across the 2-D model solution (Figure 6). In the third method, each depth point was determined independently by applying the spike approach to the columns of the velocity mesh in succession. Green bars in Figure 8 denote the median average depth of the layer 2/3 boundary in the final solutions, and Figure 9 presents the final decomposition of the velocity models into layers 2 and 3.

7. Results

[19] The preferred model solutions for each refraction line are shown in Figure 6. Image intensity is regulated by the derivative weight sum (DWS), which estimates ray density with a hit count that weights each ray by its distance to the model parameter. Whitespace corresponds with poorly constrained regions where DWS< 1.0. Figure 7 presents ray diagrams and traveltime plots illustrating the fit between pick times (black vertical

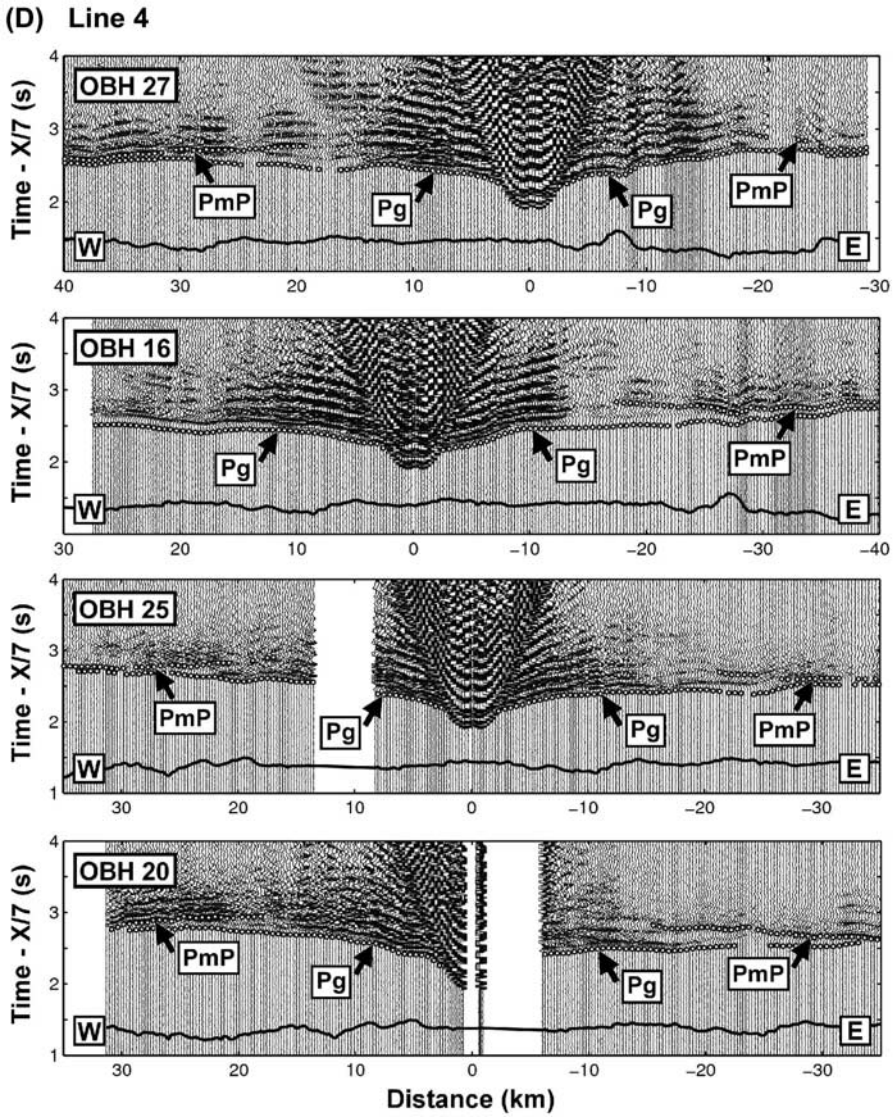

Figure 3. (continued)

bars) and synthetic traveltimes predicted by the final model solutions (red dots). Median-averaged 1-D velocity models for lines 2, 4, 5, and 6 appear in Figure 8. Summary statistics for all six lines are listed in Table 3, including the analysis bounds used to avoid poorly sampled regions near the model edges when averaging across the 2-D velocity models.

7.1. Segment P1 (Lines 1 and 2)

[20] Instrument records for line 1 show a rapid attenuation of *P* wave arrivals at ranges of 10–15 km (Figure 3a), indicating the presence of a melt lens beneath the segment P1 axial high. The distribution of Pg ray turning depths in the line 1 solution (Figures 6a and 7a) places the lens at ~1.5 km bsf, which is consistent with the estimated depth to the melt lens reflector (1480 m bsf) imaged by the coincident MCS shot line [*Baran et al.*, 2005]. PmP phase arrivals were masked by melt in the crust, so no on-axis thickness estimate could be determined.

[21] The high SNR of data collected off-axis along line 2 (Figure 3b) accommodated the identification of 1403 traveltimes picks (Pg and PmP), some at source-receiver ranges in excess of 40 km. Crustal thickness in our preferred model (Figure 6b) is 6.1 km on average and reaches a maximum of 6.3 km at the peak of a mild dome-like thickening located near 100°42′E (Figures 6b and 9a). Layer 2 exhibits a nearly constant thickness of ~2.1 km along the survey line (Figure 9a). Thickening

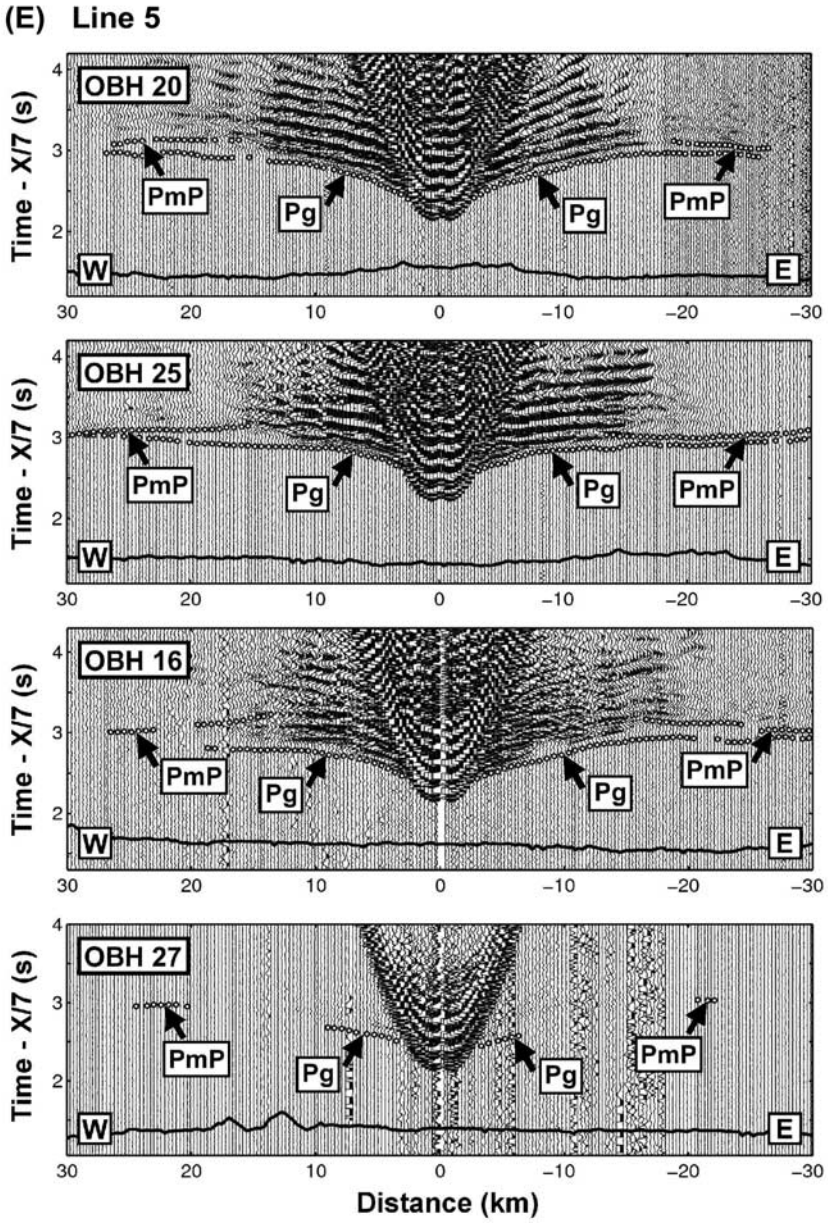

Figure 3. (continued)

predominantly occurs in layer 3 and directly parallels the inflated section of the P1 axial high (Figures 2a and 9a), consistent with lower crustal growth due to enhanced melt supply.

7.2. Segment P2 (Lines 3 and 4)

[22] Line 3 record sections display both melt-related signal loss and, on occasion, discernible far-offset PmP arrivals (Figure 3c), reflecting the deeper and more intermittent character of the axial melt lens relative to segment P1 [*Baran et al.*, 2005]. The majority (>94%) of refracted rays turn no deeper than 2.3 km bsf (Figure 7c, top), close to where a lens reflector appears in MCS data (2100 m bsf) [*Baran et al.*, 2005]. Estimates of crustal thickness using PmP reflections depend on certain assumptions regarding lower crustal structure, e.g., nearly constant, low-amplitude gradients with little lateral variations in velocity. When combined with the inherent velocity-depth ambiguity, a common complication arising from the lack of refraction constraints on deeper velocity structure, the presence of a low-velocity zone (LVZ) greatly increases the level of nonuniqueness associated with solutions to the inverse problem.

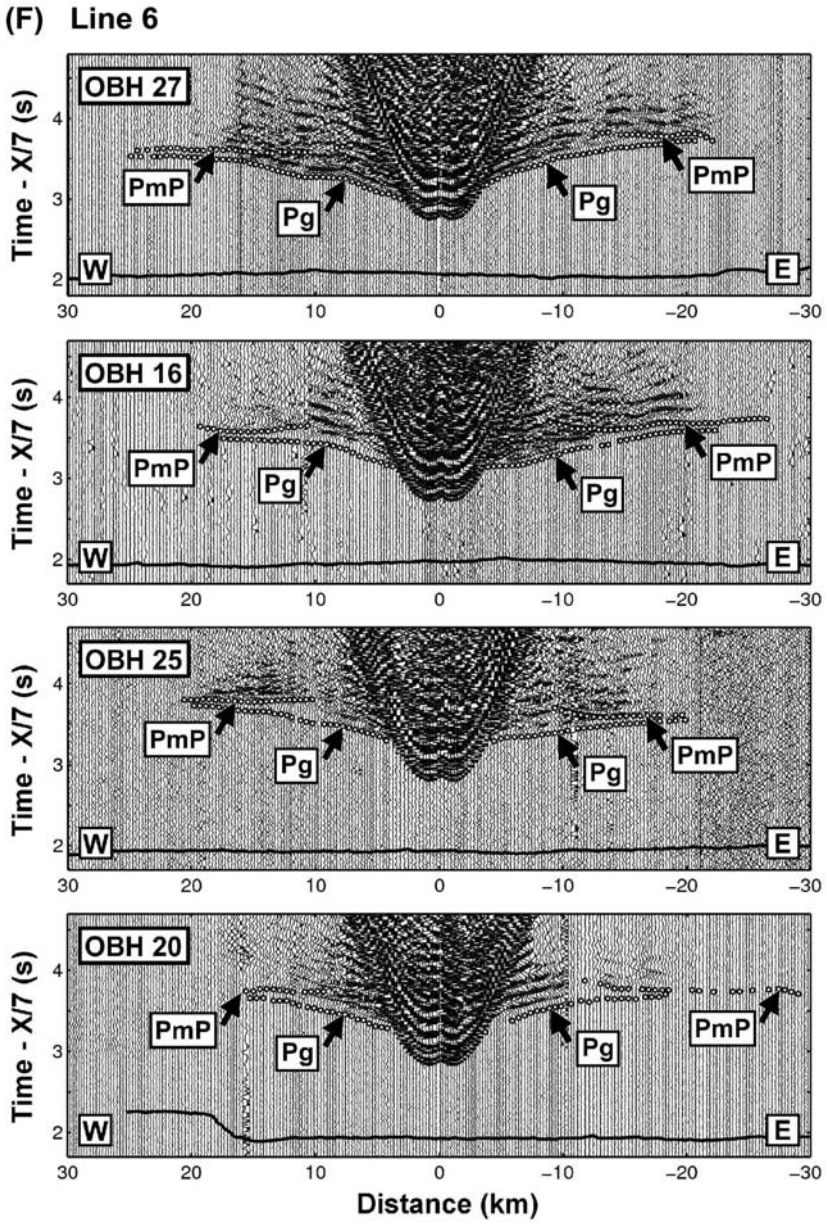

Figure 3. (continued)

Our minimum structure approach solves for the smoothest model that fits the data, favoring models with a deeper Moho over those with sharp velocity gradients in the lower crust. For example, the solution in Figure 6c (top) fits the data well ($\chi 2$ = 0.98), but the estimated crustal thickness (6.8 ± 0.4 km) is significantly greater than the observed within the more robust segment P1, suggesting the line 3 reflector was overperturbed in order to fit PmP arrivals to the east. When depth perturbations are down-weighted relative to velocity perturbations (w = 0.01), the outline of a negative anomaly is recovered between OBHs 16 and 27, but the absolute P wave velocities within the LVZ greatly exceed realistic expectations (i.e., v_p should approach ~2.5–3.0 km/s near the subaxial melt lens [*Murase and McBirney*, 1973; *Vera et al.*, 1990]). Although solutions with thinner crust would be possible with a more pronounced negative anomaly, we find this model represents the minimum thickness solution (6.0 ± 0.2 km) as long as no predefined anomaly is superimposed on the starting model. Given the high degree of uncertainty associated with modeling this shot line, we refrain from further analyzing the on-axis crustal structure along segment P2.

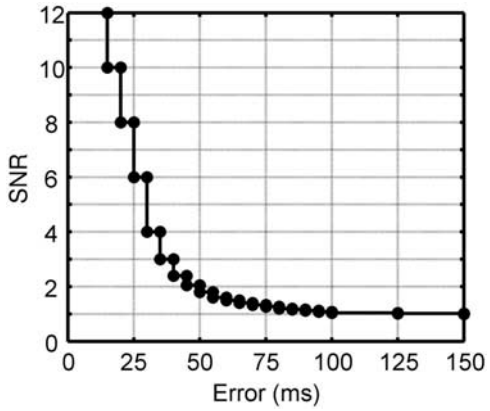

Figure 4. Empirical relationship mapping signal-to-noise ratio (SNR) of a seismic trace to the estimated uncertainty of a traveltime pick, fashioned as a stepwise variant of the complementary error function bounded by extremal values of 15 and 150 ms. The SNR is the square root of the ratio between the sample variance in the 250 ms windows following (signal) and preceding (noise) a first-arrival traveltime pick [*Zelt and Forsyth*, 1994].

[23] Line 4 traveltime data comprises a total of 1555 picks spanning shot ranges out to 40–50 km in spite of SNR variations attributable to storm-related gun-tangling (Figure 3d). Our preferred model solution exhibits a crustal thickness of 5.9 ± 0.4 km (Figures 6d), with median-average seismic layer 2 and layer 3 thicknesses of ~2.6 and 3.4 km, respectively. Assuming crustal production has remained approximately constant between lines 3 and 4, this thickness result is further evidence for thinner crust and low velocities in the lower crust beneath line 3. Although line 4 crustal thickness remains nearly constant west of ~100°57′E, layer 3 domes by ~0.6 km in a trade-off with layer 2, reaching a maximum thickness of ~3.9 km near ~101°37′E (67.5 km mark, Figure 9c). This particular section of line 4 parallels a broad shoaling of the ridge axis (between OBHs 16 and 20 on line 3, Figure 2b), suggesting that layer 3 thickens on-axis in response to a locally enhanced supply of melt. Layer 2 thickens at the expense of layer 3 to the west where the shot line crosses off-axis traces of the 101°30′E OSC (Figures 2b and 9c), possibly indicating a decrease in crustal velocities due to extensive fracturing and serpentinization associated with the discontinuity.

7.3. Segment S1 (Line 5)

[24] The absence of a melt lens reflector in MCS data collected along segment S1 [*Baran et al.*, 2005] suggests the systematic regional increase in axial depth and bathymetric roughness, not interstitial melt, causes the notably reduced SNR in line 5 records relative to data collected to the west (Figure 3e). Crustal thickness is 5.2 ± 0.6 km based on the inversion of 899 traveltime picks. Our preferred model (Figure 6e) resolves crustal thinning west of ~109°29′E toward the 108°30′E transform complex that is primarily focused in layer 3 (Figure 9d). A gradual but more substantial degree of thinning takes place east of ~109°29′E toward the tip of the 111°E PR, deviating only near OBH 20 (~110°E) where the axial valley mildly narrows and shallows in a hourglass-like shape (Figure 2c). These thinning trends suggest a waning of available melt supply near segment ends as has been noted along segments of the MAR [e.g., *Tolstoy et al.*, 1993; *Canales et al.*, 2000].

7.4. Segment T (Line 6)

[25] The depth and rigosity of the segment T axial valley together with the storm-related loss of more than half the source array greatly reduced the signal quality observed in line 6 record sections (Figure 3f), limiting picks to ranges no greater than 20–30 km. Our preferred velocity model (Figure 6f, top) displays a crustal thickness of 4.6 ± 0.8 km. Although rays reach turning depths of ~3.9 km bsf when traced through this model (Figure 7f, top), the sparseness of the data (845 picks) introduces a greater level of nonuniqueness to the model solution compared with the other

Table 2. Inversion Parameters

Line	L_{vh}	L_{vv}	L_d	λ_v	λ_d	α_v	α_d	w
1	2.0/25.0	0.05/2.5	5.0	5.0	N/A	50/75/150	25.0	1.0
2	2.0/25.0	0.05/2.5	5.0	5.0	10.0	50/100/200	25.0	1.0
3	1.5/20.0	0.05/2.0	5.0	5.0	10.0	50/75/100	25.0	1.0
4	2.0/25.0	0.05/2.5	5.0	5.0	10.0	50/100/200	25.0	1.0
5	2.0/25.0	0.05/2.5	5.0	5.0	10.0	50/75/100	25.0	1.0
6	1.5/20.0	0.05/2.0	5.0	5.0	10.0	50/75/100	25.0	1.0

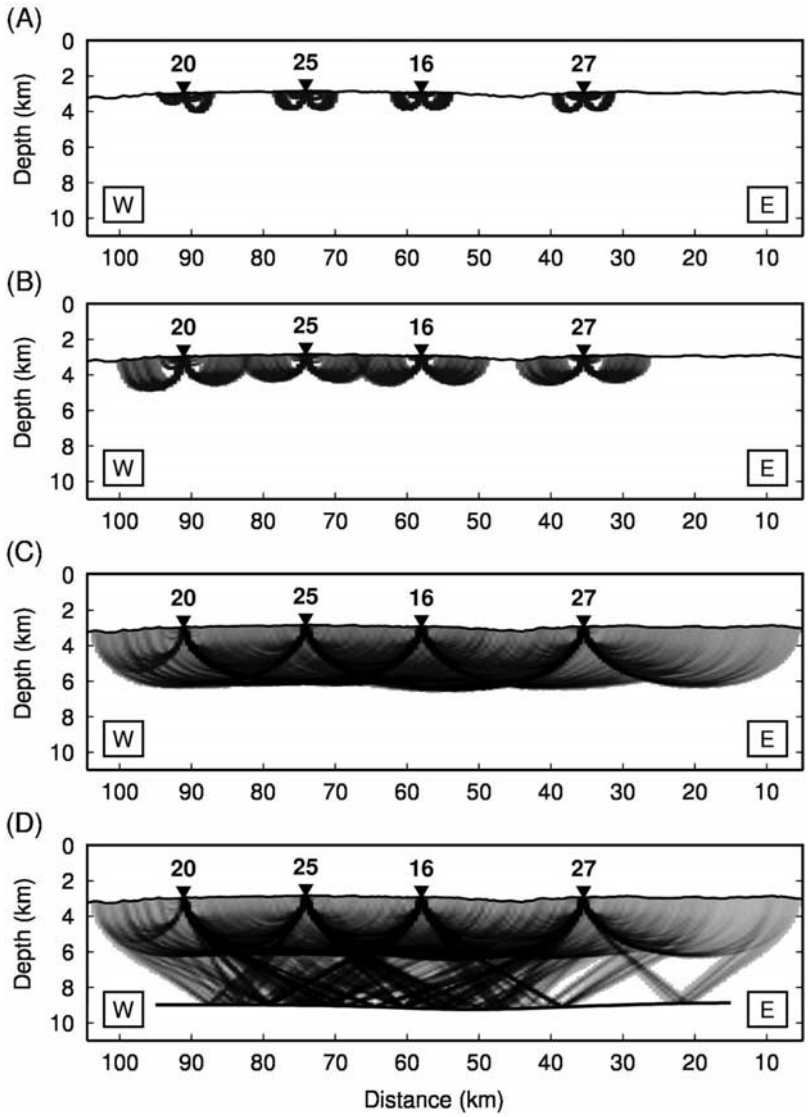

Figure 5. Illustration of the top-down inversion methodology. Image intensity is scaled by the derivative weight sum (DWS) to emphasize the systematic increase in model constraints. (a) Step 1: input data are restricted to Pg picks at source-receiver offsets ≤5 km. (b) Step 2: only Pg picks at offsets ≤10 km are included. (c) Step 3: the full Pg data set is used with no offset restrictions. (d) Step 4: all Pg and PmP traveltime data are inverted. The reflector is denoted by the solid line.

refraction line inversions. We performed a trial inversion with w reduced to 0.01 in order to test the possible influence of the velocity-depth ambiguity. The resulting model (Figure 6f, bottom) is characterized by a crustal thickness of 4.5 ± 0.2 km, indicating our median average thickness results are robust. Layer 3 and total crustal thickness jointly decrease west of ~114°40′E (80 km mark, Figure 9e, top), suggesting that melt supply decreases toward the 114°E transform. Crustal thickness also decreases to the east, reaching a minimum of ~3.8 km in the vicinity of a conspicuous left step in the axial valley (~114°45′E, Figure 2d). The ridge axis simultaneously deepens to ~4.5 below sea level (bsl) (Figure 9e, top), the maximum depth along the refraction line, suggesting the valley jog is a noteworthy segmentation boundary even with an absolute offset of <5 km (Figure 2d). Crustal thickness and seafloor topography increase eastward to 115°07′E where the axial valley forms an hourglass shape, narrowing by half and shallowing to ~4.0 km bsl (Figure 2d). The w = 0.01 solution differs from the w = 1.0 case east of this point; when w = 1.0, crustal thickness remains nearly constant (~5.0 km) even near the tip of the 116°E stalled PR, but the w = 0.01 solution shows crustal thinning as layer 3 effectively disappears by the 20 km mark (~115°28′E, Figure 9). A similar structural

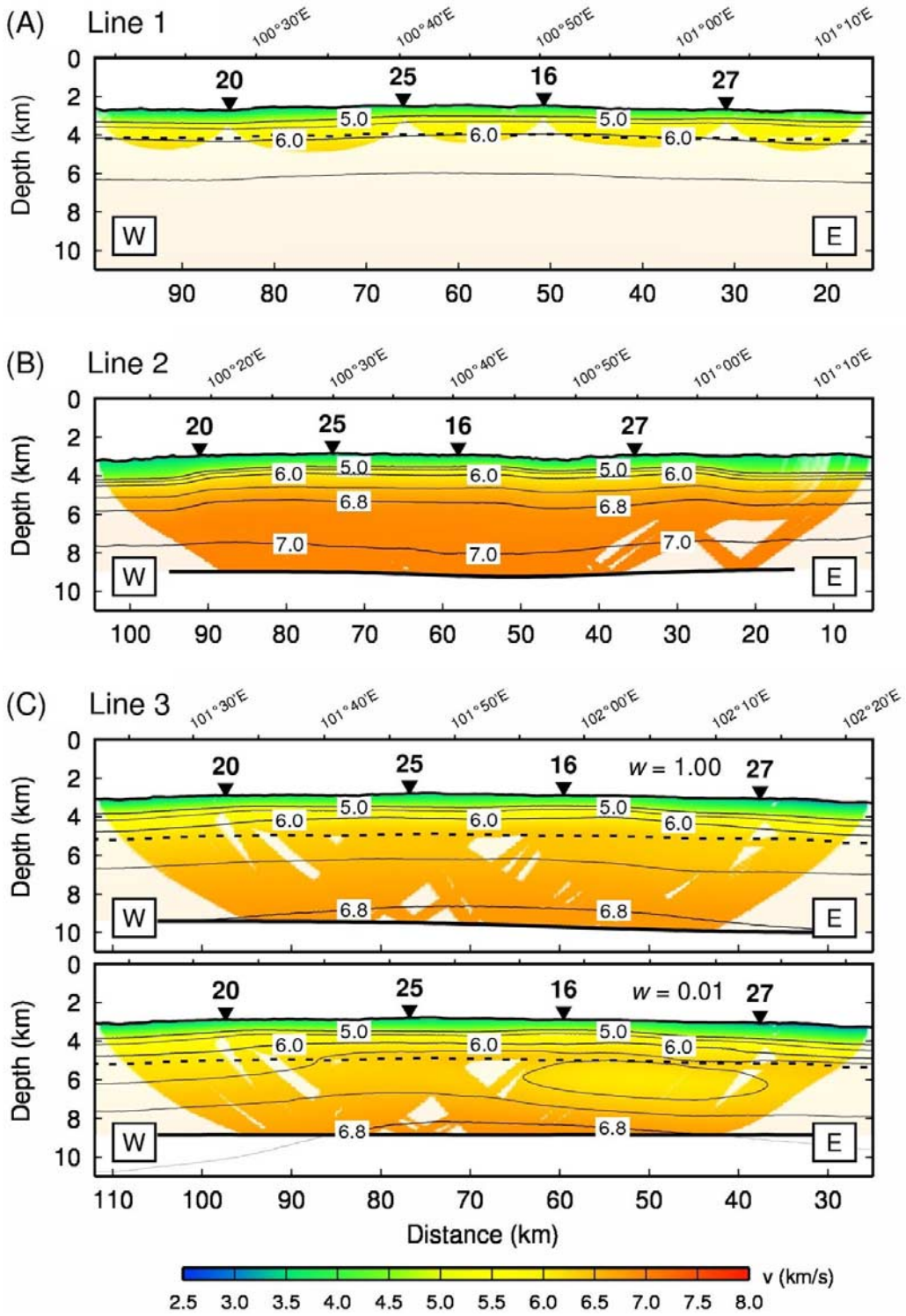

Figure 6. (a–f) Preferred model solutions for each refraction line. The contour interval is 0.5 km/s for velocities ≥5.0 km/s. The 6.8 km/s contour is also shown. Axes describe depth bsl and along-line distance in both km and longitude (°E). Unconstrained regions of the velocity model are masked by scaling the image intensity with the DWS. The preferred solution reflector (solid) is superimposed on the velocity surface. Average depth to the axial melt lens [from *Baran et al.*, 2005] is indicated by a dashed line in Figures 6a and 6c. Figures 6c and 6f also show the solution when the depth kernel weighting factor is set to w = 0.01.

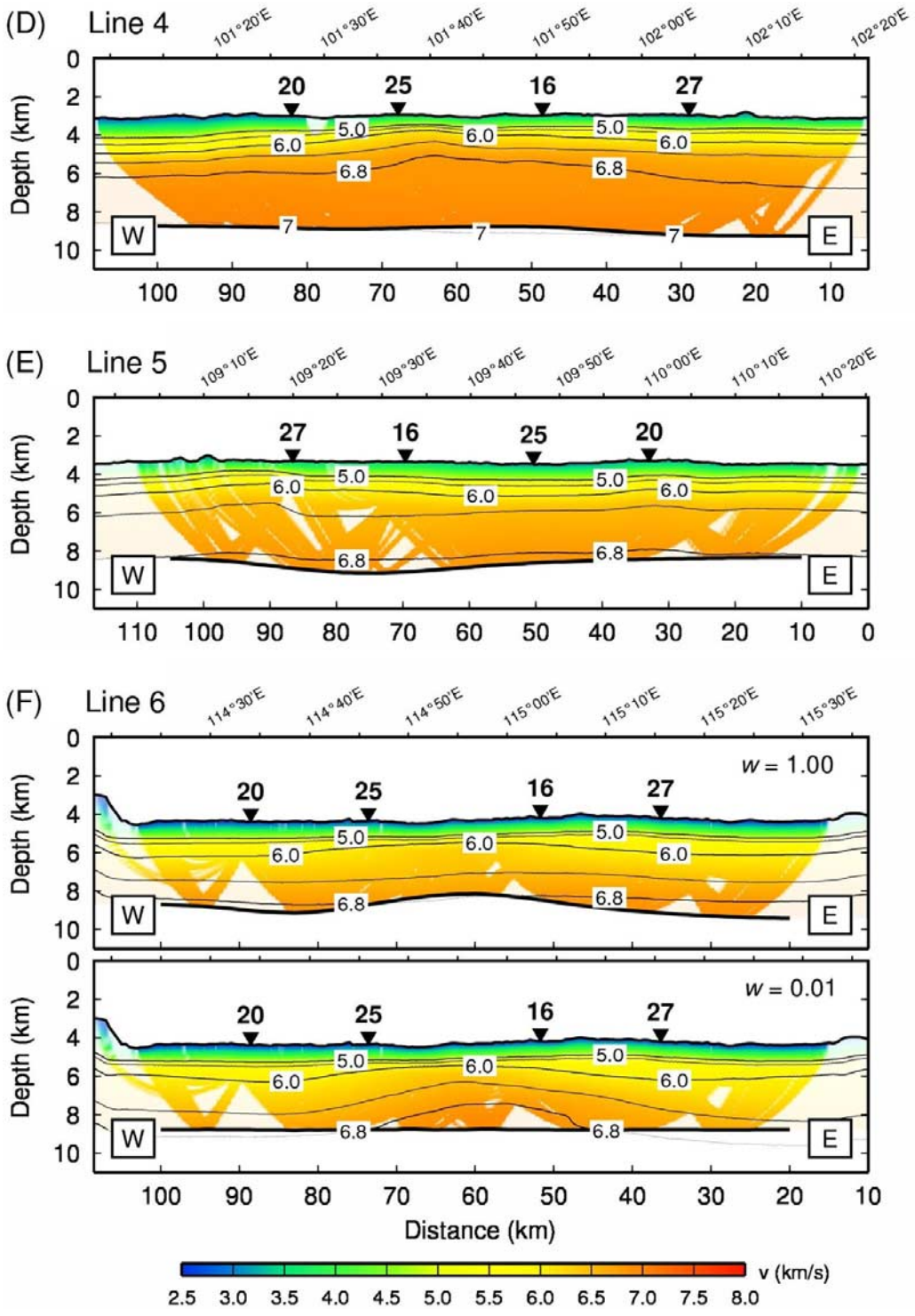

Figure 6. (continued)

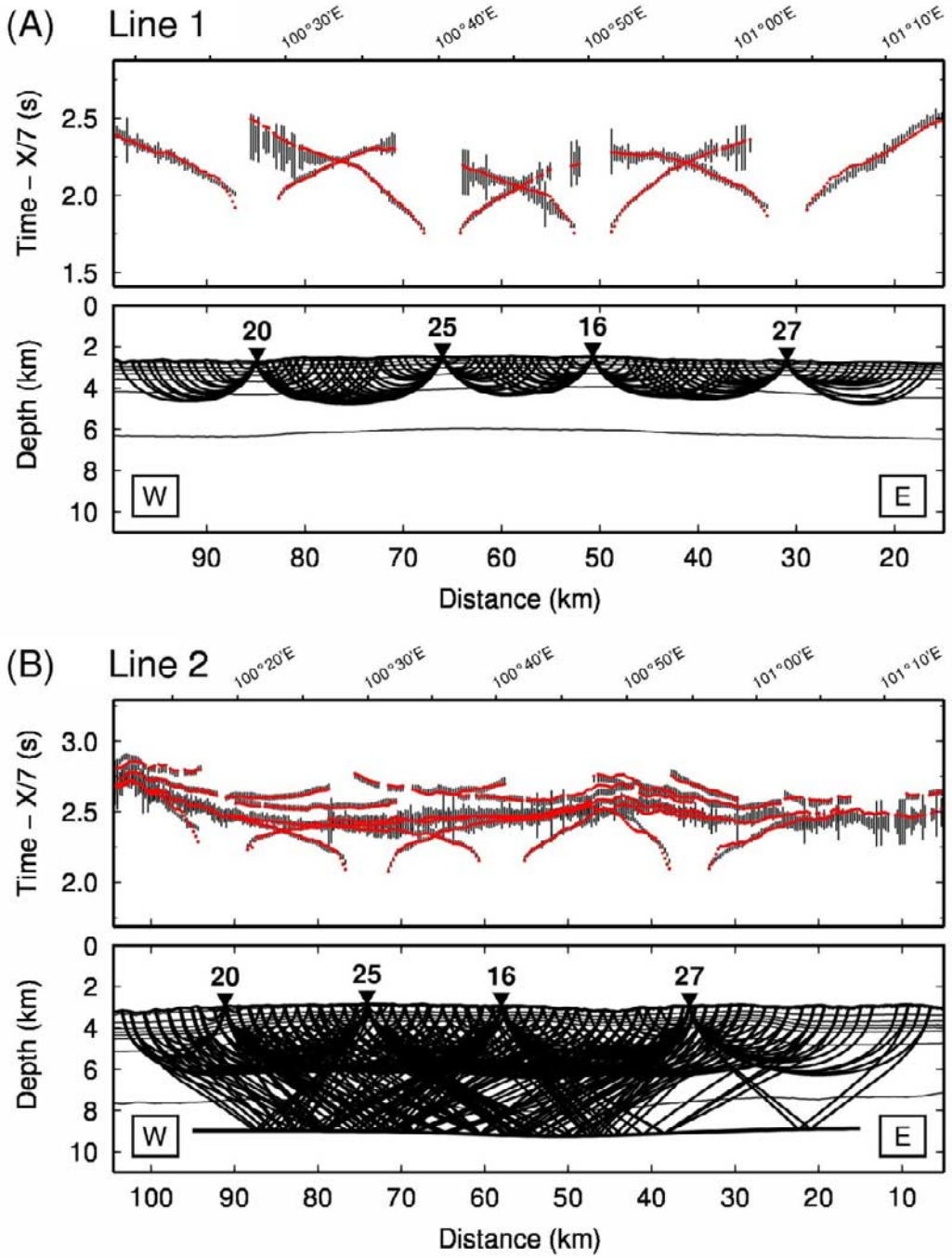

Figure 7. (a–f) Ray coverage and data misfit for the preferred velocity models. The vertical axis in Figures 7a–7f (top) measures two-way traveltime reduced to 7 km/s. Gray vertical bars depict Pg and PmP picks. Bar length is equivalent to the $\pm 2\sigma_e$ (95%) confidence interval, where σ_e is the SNR-based pick error estimate. Traveltimes predicted from the model solutions are superimposed in red. Figures 7a–7f (bottom) trace the corresponding raypaths with depth bsl. Figures 7b, 7d, and 7e show every fifth ray, while Figures 7a, 7c, and 7f show every third ray for figure clarity.

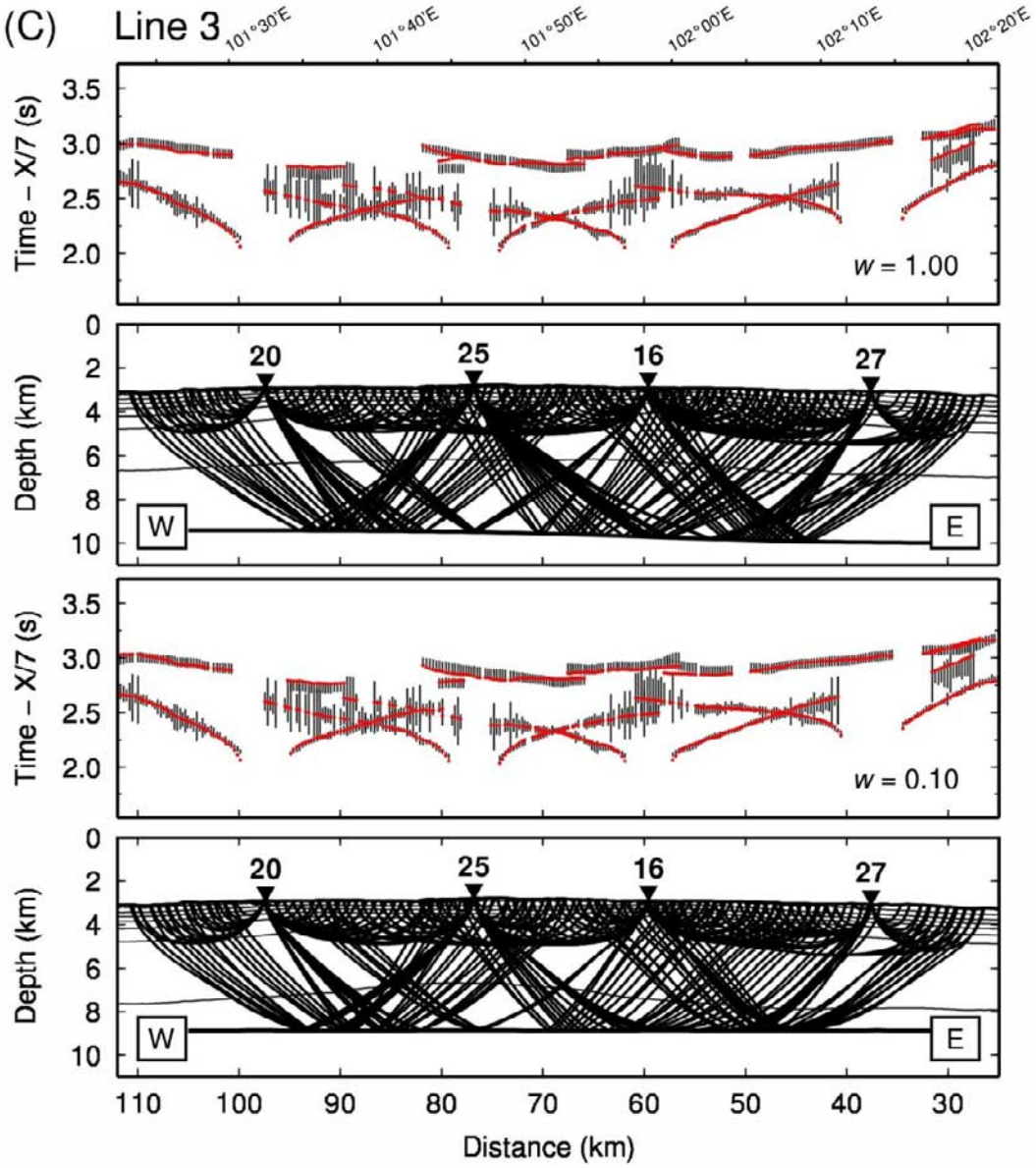

Figure 7. (continued)

dichotomy exists near the 114°45′E discontinuity, due to the bias against perturbing the flat reflector when $w = 0.01$ (Figure 9). Despite these differences, the solutions share two fundamental features: the average crustal thickness remains approximately the same and the 114°45′E discontinuity marks a sharp change in crustal structure.

8. Discussion

8.1. Crustal Thickness Variations

[26] The most striking characteristic of the tomography results is the systematic decrease in crustal thickness from west to east along the 100°–116°E section of the SEIR (Figure 10). With the exception of the ultraslow class of ridges (<15 mm/a) [e.g., *Minshull et al.*, 2006; *Jokat and Schmidt-Aursch*, 2007], studies show crustal thickness is independent of spreading rate [*Chen*, 1992; *Bown and White*, 1994]. The average thickness of oceanic crust is ~7 km away from hot spots, fracture zones, and other anomalous influences [*White et al.*, 1992] and drops to 6.0–6.5 km when fracture zone crust is included [*Chen*, 1992; *Bown and White*, 1994]. By these measures, the SEIR exhibits normal or near-normal crustal thickness at segments P1 (6.1 km) and P2 (5.9 km), but has unusually thin crust at segments S1 (5.2 km) and T (4.6 km).

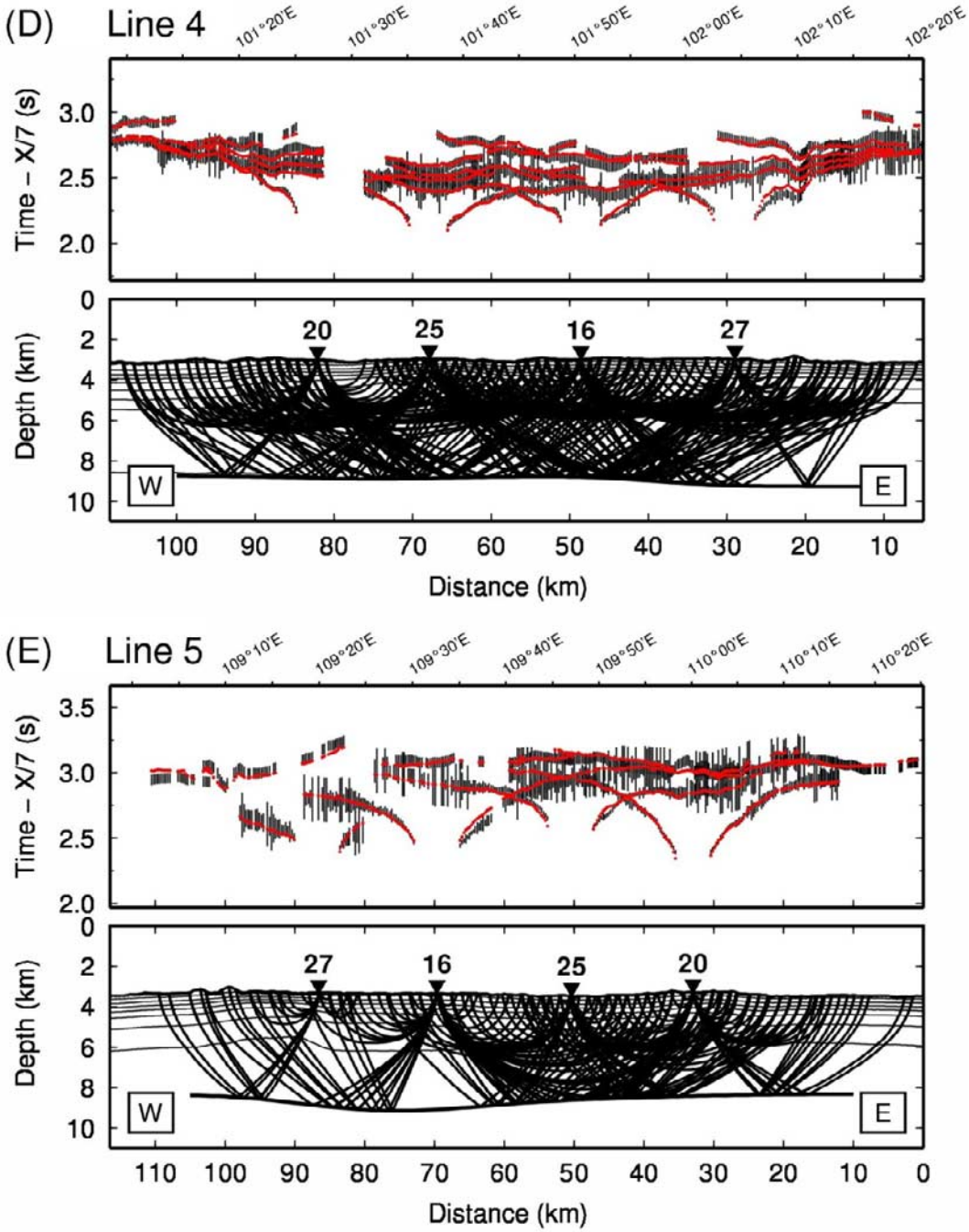

Figure 7. (continued)

8.2. Mantle Temperature Variations

[27] Assuming that mantle upwelling along the SEIR is simply a passive response to plate divergence, the two primary factors governing variations in melt supply and, hence, crustal thickness are mantle geochemistry, which is consistently Indian-MORB-type to the west of the AAD [*Klein et al.*, 1991; *Mahoney et al.*, 2002], and the thermal conditions in the upper mantle. Basaltic glasses collected along the SEIR between 86° and 118°E display an inverse Na_8-Fe_8 correlation indicative of a systematic cooling trend in the asthenosphere directed toward the AAD [*Mahoney et al.*, 2002; J. M. Baran et al., Constraints on the mantle temperature gradient along the Southeast Indian Ridge from crustal structure and isostasy: Implications for the transition from an axial high to an axial valley, manuscript in preparation for *Geophysical Journal*

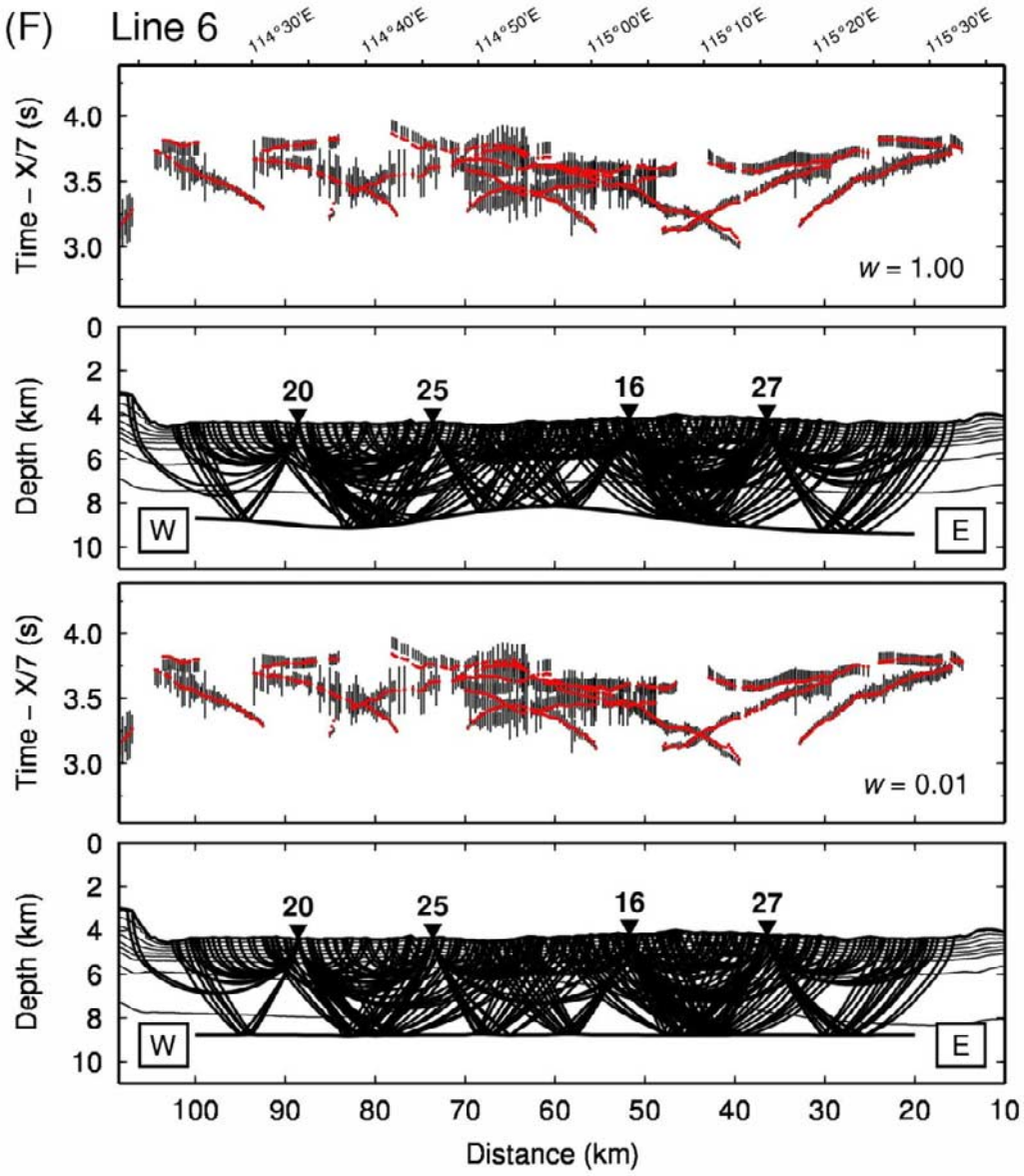

Figure 7. (continued)

International, 2008]. Following the methods of Baran et al. (manuscript in preparation, 2008), we calculated the magnitude of this thermal gradient using three theoretical models relating mantle temperature to melt supply (crustal thickness): the *McKenzie* [1984] isentropic upwelling model; the polybaric melting column model of *Klein and Langmuir* [1987]; and the *Chen* [1996] model combining 2-D corner flow with fractional melting. On the basis of our average crustal thickness results for segments P1 and T, these models predict a mantle temperature difference of 33°C, 30°C, and 28°C, respectively (Figure 11), which is consistent with the temperature change required by residual gravity anomaly and ridge flank depth variations observed across the study region (25°–50°C) [*Shah and Sempéré*, 1998]. Using the least squares great circle fit to the shot data for all on-axis lines to calculate the distance between the midpoints of segments P1 and T, we estimate the average mantle temperature gradient between 100° and 116°E to be approximately −2.8°C/100 km to the east.

8.3. Transitional Behavior

[28] Segments P2 and S1 lie to either side of the transition from an axial high to an axial valley, indicating this fundamental change in morphology occurs over a very small range of thickness values (∼5.2–5.9 km). A similarly rapid transition is

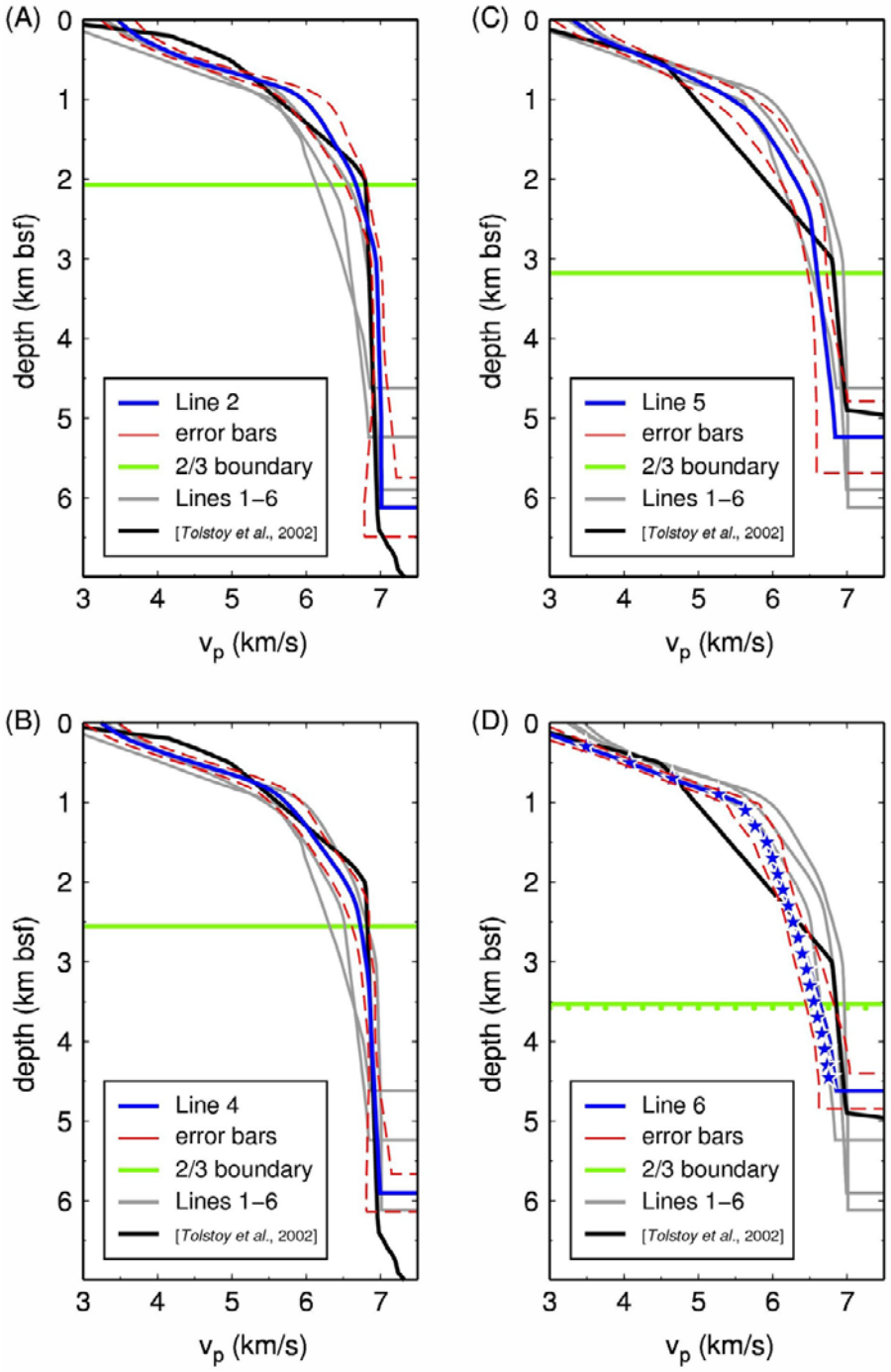

Figure 8. (a–d) One-dimensional median-average velocity-depth profiles from the preferred model solutions for lines 2, 4, 5, and 6. Depths are measured below seafloor (bsf). Each plot shows the results for the four refraction lines (gray); the specific profile of interest (blue); the starting model based on forward-modeling results from *Tolstoy et al.* [2002] (black); the median-average depth of the layer 2–3 boundary (green); and 95% confidence intervals for both velocity and crustal thickness (red dashed) determined from Monte Carlo analysis. Blue stars and the green dotted line in Figure 8d depict the median-average profile and layer 2–3 boundary when w = 0.01.

Table 3. Results of Inversions

Line	1	2	3[a]	3[b]	4	5	6[a]	6[b]
Pg pick count	392	922	440	440	934	544	525	525
PmP pick count	0	481	277	277	621	355	320	320
Analysis bounds[c]	20–95	15–95	30–105	30–105	10–100	10–100	20–100	20–100
Median crustal thickness, km	N/A	6.1	6.8	6.0	5.9	5.2	4.6	4.5
Standard deviation[d], km	N/A	0.1	0.2	0.1	0.2	0.3	0.4	0.1
Median layer 2 thickness, km	N/A	2.1	4.0	5.1	2.6	3.2	3.5	3.6
Median layer 3 thickness, km	N/A	4.0	2.7	0.8	3.4	2.1	1.0	0.9
Initial RMS error, ms	61.6	117.6	127.4	127.4	74.0	159.0	79.9	79.9
Initial χ2 misfit	7.19	28.29	27.50	27.50	9.14	27.79	5.56	5.56
Final RMS error, ms	27.7	22.0	29.1	29.7	27.2	30.1	33.0	33.4
Final χ2 misfit	0.99	0.99	0.98	0.98	1.00	0.98	1.00	1.00

[a] Using w = 1.00.
[b] Using w = 0.01.
[c] Defines regions used for calculating median thickness values.
[d] Represents across-model variability, not standard error.

observed at the intermediate-spreading (~50 mm/a) GSC, where axial topography changes from a rifted high to an axial valley as crustal thickness decreases from ~5.9 to 5.6 km [*Canales et al.*, 2002]. In the slow-spreading 8°–9°S section of the MAR (32–33 mm/a), the high-to-valley transition occurs at a significantly greater crustal thickness (~8 km) [*Minshull et al.*, 2003]. This is consistent with global trends that show a rate-dependent correlation between ridge morphology and axial depth; morphological changes occur at slower spreading rates where the ridge axis is shallow, or by rough proxy, where crust is thick [*Malinverno*, 1993]. Transitions from axial high to rifted high at the 101°30′E OSC (Figures 2a–2b) and from shallow valley to deep rift valley at the 114°E transform (Figures 2c–2d) are likewise very sensitive to changes in crustal thickness given the small intersegment variations observed between P1 and P2 (~0.2 km) and between S1 and T (~0.6 km).

[29] Thermomechanical models for axial topography [e.g., *Chen and Morgan*, 1990a, 1990b] have demonstrated a threshold-type dependence of ridge morphology on both spreading rate and the underlying thermal structure of the ridge (i.e., mantle temperature and crustal thickness), which is well-supported by the abrupt valley-no rift valley transition accompanying the ~0.7 km decrease in crustal thickness between P2 and S1. Seismic studies indicate the systematic inverse relationship between spreading rate and the position of the axial melt lens behaves in a similar fashion; the melt lens, which generally lies 1.2–1.8 km bsf at spreading rates of 85–155 mm/a, rapidly deepens with decreasing spreading rate once an intermediate rate threshold value (<85 mm/a) has been crossed [*Purdy et al.*, 1992; *Carbotte et al.*, 1998]. The crustal genesis model of *Phipps Morgan and Chen* [1993a, 1993b] predicts that at any given spreading rate, small variations in melt supply (crustal thickness) will produce threshold-type changes in the depth to the "solidus" freezing horizon and, consequently, the depth of the melt lens. Our results support this model: the median-averaged crustal thickness for line 2 differs from line 4 by only ~0.2 km, yet the melt lens deepens from 1480 to 2100 m bsf [*Baran et al.*, 2005]. And although a reflector is imaged 2900 m bsf within the adjacent segment R, a lens is absent beneath segment S1 [*Baran et al.*, 2005] presumably because the solidus has crossed the crust-mantle boundary in conjunction with the <1 km decrease in crustal thickness from P2 to S1.

8.4. Crustal Unit Variations

[30] It is a broadly accepted practice to discuss crustal structure in terms of the classic three-layer framework: a low-velocity layer of accumulated sediments (layer 1) generally absent at mid-ocean ridges due to their young age, an upper igneous layer with steep velocity gradients (layer 2), and a generally thicker, low-gradient igneous layer bounded by the Moho (layer 3) [*Raitt*, 1963; *Houtz et al.*, 1970; *Talwani et al.*, 1971]. Ophiolite exposures show a similar stratification, where a basaltic upper layer of extrusives and dikes lies above a thicker, more homogeneous section of layered gabbros [*Christensen and Smewing*, 1981; *Hopson et al.*, 1981]. The direct correspondence between seismic and lithological crustal units has been challenged by Ocean Drilling Program (ODP) studies at Hole 504B [*Detrick et al.*, 1994] and Hole 1256D [*Wilson et al.*, 2006].

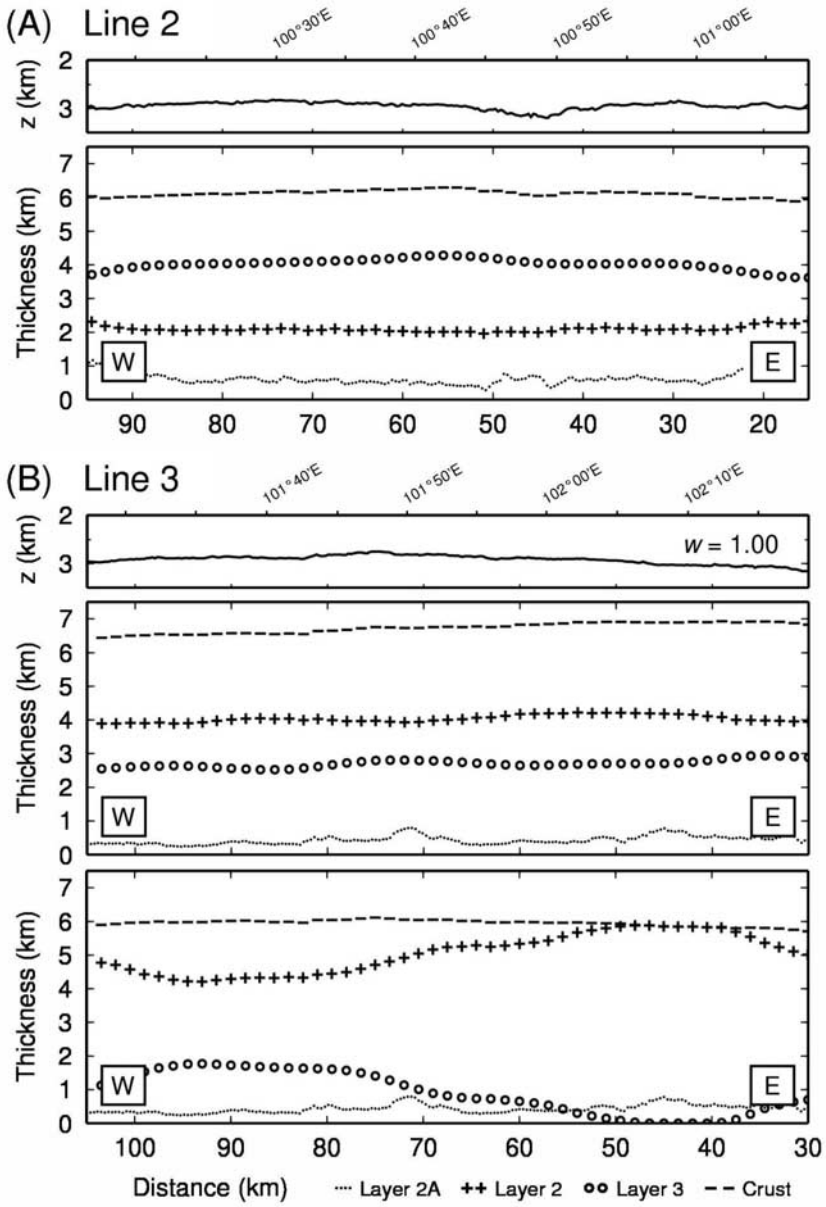

Figure 9. (a–e) Crustal unit thickness variations in the preferred model solutions. The horizontal axis displays distance in (bottom) kilometers and (top) degrees longitude (°E). Along-line bathymetry (Figure 9, top) is measured in depth bsl. Crustal thickness (dashed) is subdivided into seismic layer 2 (pluses) and layer 3 (circles) based on the decrease in vertical velocity gradient defining the layer 2–3 boundary. Layer 2A thickness estimates (dotted) come from a separate analysis of MCS data [*Baran et al.*, 2005]. Figures 9b and 9e also present thickness results when depth perturbations are suppressed using a depth kernel weighting factor of w = 0.01.

However, borehole depth limitations at 504B led investigators to rely on extrapolated velocity trends, and while gabbros first appear above the seismic layer 2/3 boundary at 1256D, the top of the plutonic complex is at the depth predicted by regional seismic measurements. We have chosen to analyze our results in context of the seismic layer representation for its convenience and simplicity. Nevertheless, care must be taken in interpreting all velocity variations as petrologic in nature.

[31] Refraction experiments conducted above "normal" oceanic crustal (i.e., nonhot spot, MOR-derived) indicate layer 2 averages 1–3 km in thickness, while layer 3 is typically 4–6 km thick

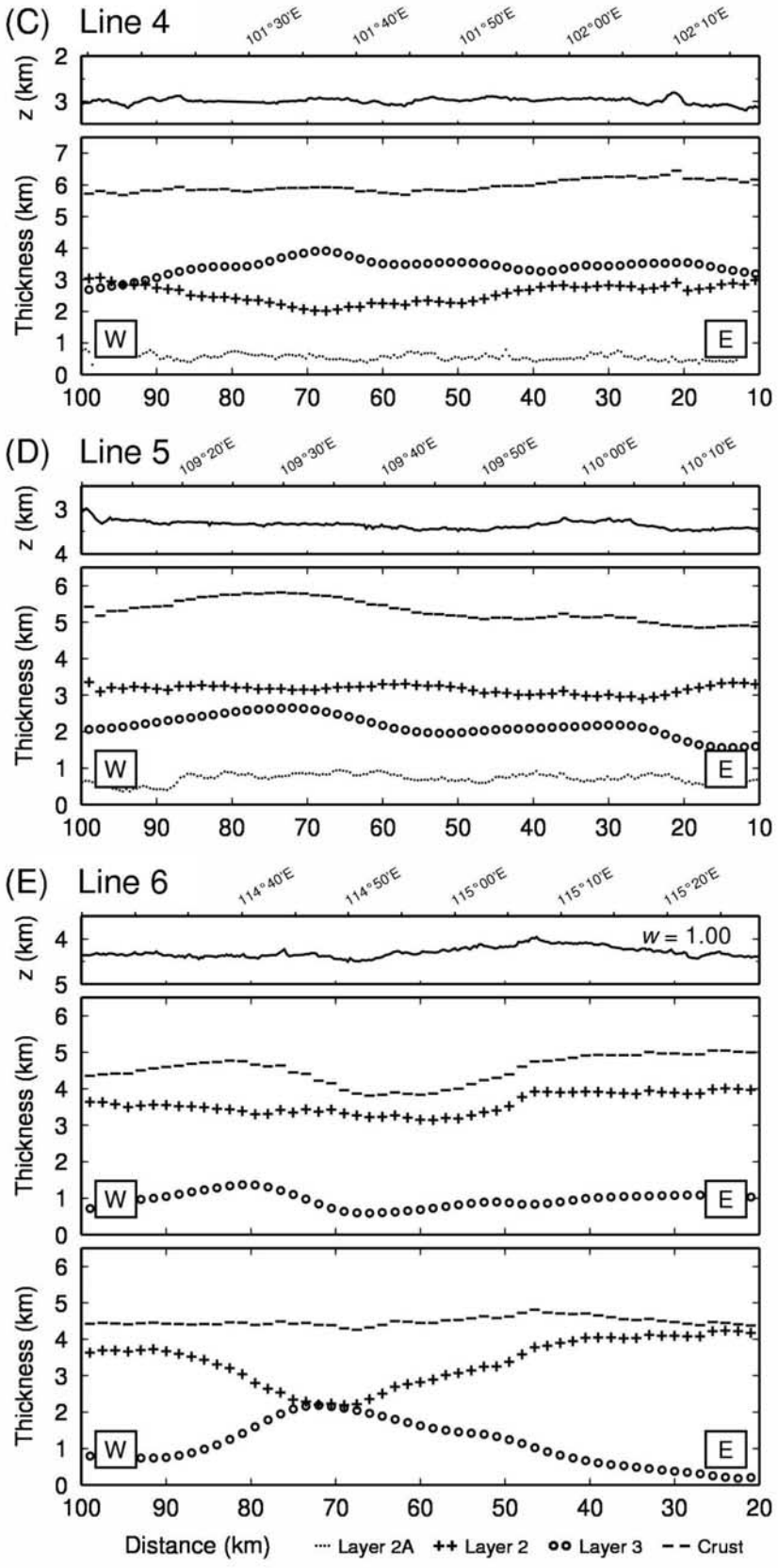

Figure 9. (continued)

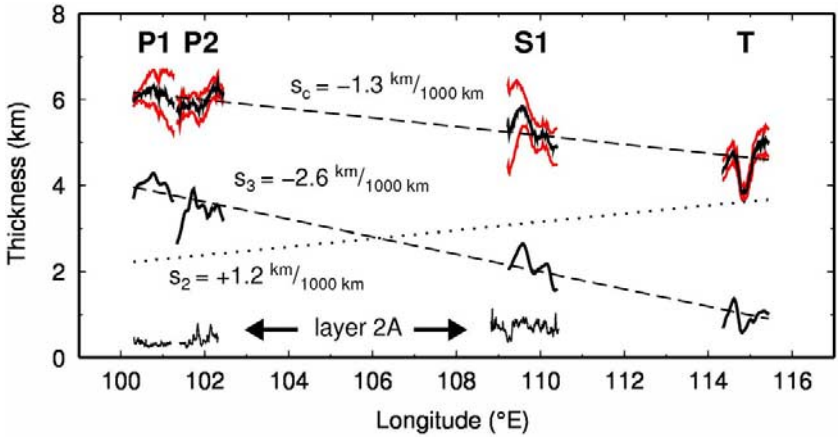

Figure 10. Thickness variations of crustal units across the study area. (top) Total crustal thickness for segments P1, P2, S1, and T is plotted with 95% confidence intervals (red) derived from Monte Carlo analysis. Additional thickness profiles for (middle) layer 3 and (bottom) layer 2A [from *Baran et al.*, 2005] are also shown. Least squares trend lines for layer 2 (dotted), layer 3 (dashed), and the entire crust (dashed) define linear approximations of the respective thickness gradients (annotated "s" values) along this section of the SEIR.

[e.g., *White et al.*, 1992; *Mutter and Mutter*, 1993]. Our results show a systematic decrease in layer 3 thickness from 4.0 km to 1.0 km as the crust progressively thins toward the AAD (Figure 10). Crustal thickness variations are commonly tied to changes in layer 3 thickness [*Mutter and Mutter*, 1993; *Tolstoy et al.*, 1993], the end-member example being the Gakkel Ridge where the crust thins to 1.4–2.9 km when layer 3 is completely absent [*Jokat and Schmidt-Aursch*, 2007]. Less prevalent is the concurrent ~1.4 km increase in layer 2 observed between segments P1 and T, which reveals a fundamental trade-off in seismic velocity structure associated with the regional crustal thickness trend (Figure 10). *Buck et al.* [1997] describe a similar trade-off in their model for extrusive behavior at fast- and intermediate-spreading ridges; as the overburden pressure on the melt lens increases, a greater fraction of magma will erupt as pillows and flows, causing the extrusive layer to thicken at the expense of the intrusive sheeted dike complex. Applying a similar model to the whole crust, as thermal conditions perturb the depth to the melt lens, the resulting change in overburden pressure may systematically alter the mode of crustal accretion along the ridge. Cooler temperatures to the east will cause the lens to deepen and the overburden to increase. The corresponding rise in magma pressure may favor increasingly larger eruptions that leave a smaller volume of melt behind to crystallize and form new lower crustal material. Over time, the overburden-regulated eruptive activity could build a thicker upper crustal section characterized by layer 2 velocities as both layer 3 and the whole crust decrease in thickness to the east.

9. Conclusions

[32] 1. Crustal thickness systematically decreases to the east by 1.5 km between 100° and 116°E, a section of the SEIR characterized by a nearly constant intermediate spreading rate and consistent MORB-type isotopic signature. Individual ridge segments range in thickness from 6.1 ± 0.2 km at segment P1 to 4.6 ± 0.8 km along segment T. Superimposed on the thickness gradient are major changes in axial morphology from a well-developed axial high to a deep axial valley.

[33] 2. Theoretical models of melt production require a decrease in mantle temperature of ~30°C to account for the change in crustal thickness between segments P1 and T. Assuming this change is both linear and ridge-parallel, the equivalent upper mantle thermal gradient is −2.8°C/100 km directed eastward toward the AAD.

[34] 3. Significant changes in axial morphology accompany small crustal thickness variations; the rifted axial high-shallow axial valley transition between P2 and S1 corresponds with a thickness difference of only ~0.7 km. A threshold-type sensitivity of morphology on small changes in crustal thickness and mantle temperature is consistent with models of crustal accretion where ridge topography is determined by a balance between mantle temperature, melt supply, and cooling from hydrothermal circulation.

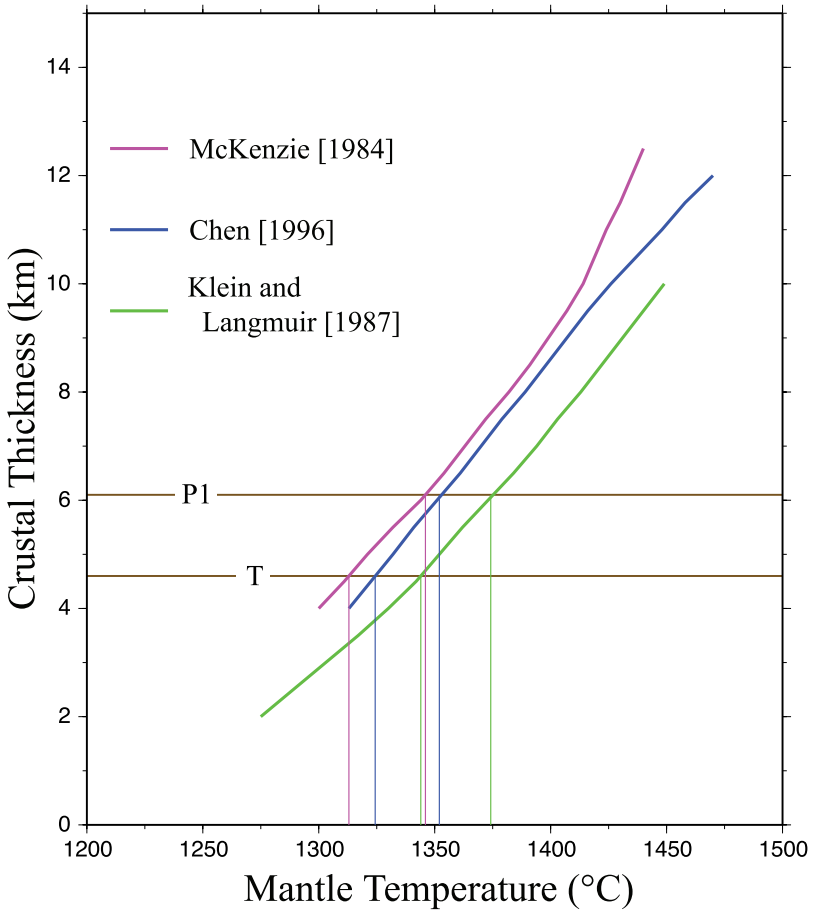

Figure 11. Theoretical calculations of crustal thickness as a function of mantle solidus temperature from Baran et al. (manuscript in preparation, 2008). The models include *McKenzie* [1984], *Klein and Langmuir* [1987], and *Chen* [1996]. Horizontal lines labeled P1 and T mark the median-average crustal thicknesses for those segments. Vertical lines show the corresponding range of mantle temperatures based on each relationship.

[35] 4. Seismic layer 3 systemically decreases by 3.0 km as layer 2 increases by 1.4 km across the study area, reflecting the eastward decrease in melt supply (crustal thickness) and the deepening of the solidus (melt lens) as axial thermal structure cools toward the AAD. Layer 3 variations control the regional trend in crustal thickness. The trade-off in seismic velocity structure may be explained by models relating overburden pressure on the melt lens to the volume and efficiency of eruptions, which could ultimately affect the relative thickness of the upper and lower crust.

Appendix A: Resolution and Uncertainty

A1. Starting Reflector Depth

[36] We examined the sensitivity of the crustal thickness results to the starting reflector by systematically varying the initial reflector depth used in the tomographic inversion for lines 2, 4, 5, and 6 (Figure A1). After completing the first three steps of the top-down technique with the same parameterization, regularization, traveltime data set, and starting velocity model used to derive the solutions in Figure 6, we combined the output with 10 test reflectors in succession and ran the forward step to determine the initial PmP traveltime misfit in each trial case. The depths chosen for the preferred starting models (circled) correspond with the minimum $\chi 2$ solutions (Figure A1a).

[37] Each curve in Figure A1b traces the difference between the trial case results and the reflector in the preferred final models (Figure 6). Solutions approach zero deviation where velocity structure is best constrained by Pg ray coverage and PmP reflections span larger, more continuous sections of the reflector. Overall, the different starting models give results that are not statistically signif-

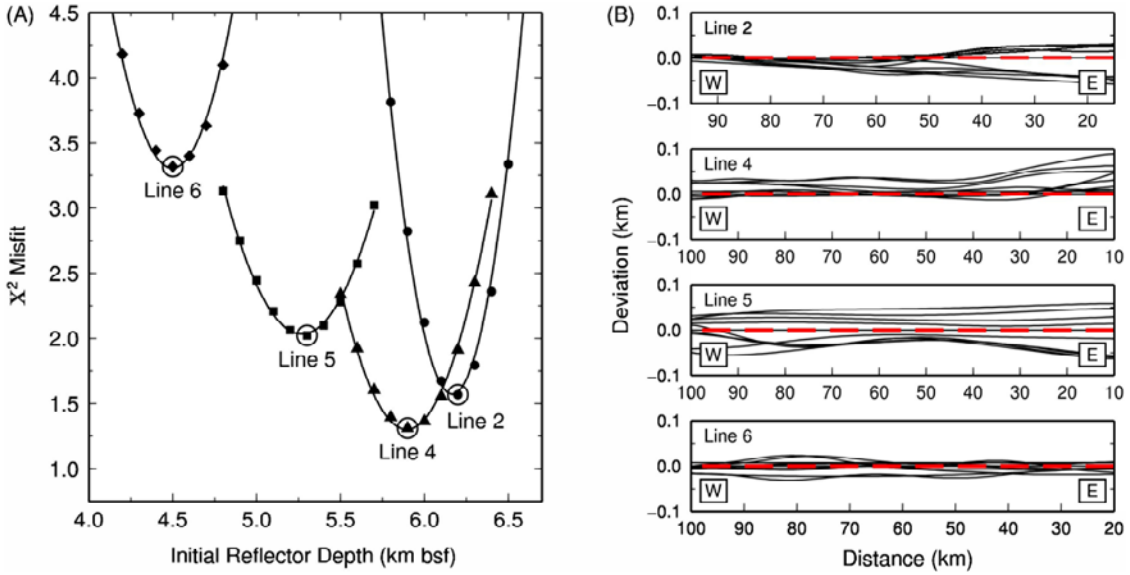

Figure A1. Solution sensitivity to the starting reflector depth. (a) Model misfit as a function of the initial depth assigned to the reflector for lines 2, 4, 5, and 6. The values of $\chi 2$ were calculated after the third step of the top-down method. The preferred starting depth (circled) lies closest to the minimum of the best fitting second degree polynomial (solid line). (b) The depth difference between test case solution reflectors and that of the preferred model solution. The red dashed line marks the zero-difference result for the preferred starting depth.

icant from one another, indicating the inversions are largely insensitive to reasonable variations in the starting reflector depth.

A2. Depth Kernel Weighting

[38] The traveltime equivalence of changing the depth to a reflector and perturbing the overlying velocity structure when fitting reflection data renders solutions to the reflection traveltime tomography problem inherently nonunique [see *Lines*, 1993; *Ross*, 1994]. Refraction data provide independent constraints on crustal velocities in marine seismic surveys; however, the progressive decrease in SNR with increasing range obscures Pg arrivals at large source-receiver offsets. The resulting gap in Pg coverage at lower crustal depths introduces a trade-off between variations in lower crustal velocities and the depth to the Moho reflector. We performed a series of inversions with different depth kernel weighting factor (w) values to test model sensitivity to this velocity-depth trade-off. The w parameter controls how the Fréchet derivatives for PmP data are weighted relative to those associated with Pg picks, biasing the inversion toward velocity perturbations when $w <$ 1.0 and depth perturbations for $w >$ 1.0 [*Korenaga et al.*, 2000]. Figure A2 presents the percent difference between trial solutions and the preferred velocity models for lines 2, 4, 5, and 6 (Figure 6) when w ranges from 0.10 to 10.0. Also plotted are the trial (solid) and preferred (dashed) reflectors.

[39] The velocity-depth trade-off is most apparent where PmP rays pass through model regions marked by sparse Pg coverage (see Figure 7). Examples include the eastern edges of lines 2, 5, and 6 as well as between 60 and 90 km along line 5 where the trial and preferred reflector solutions differ by up to ~0.3 km (Figures A2a and A2c–A2d). Line 6 exhibits the most pronounced velocity variations, reaching maximum model differences of +1% to −1.7% when w = 0.1, although the reflector depth varies by only ~0.1 km in the same model regions (Figure A2d). Outside of these specific examples, the velocity-depth ambiguity generally introduces variations in crustal thickness

Figure A2. Model sensitivity to the velocity-depth ambiguity. (a–d) The percent difference between each trial case and the preferred (w = 1.0) model solutions for lines 2, 4, 5, and 6. The contour interval is 0.2%. Test case depth kernel weighting factor values include w = 0.1, 0.5, 2.0, and 10.0. Superimposed are the reflectors from the trial solution (solid) and the preferred final model (dashed).

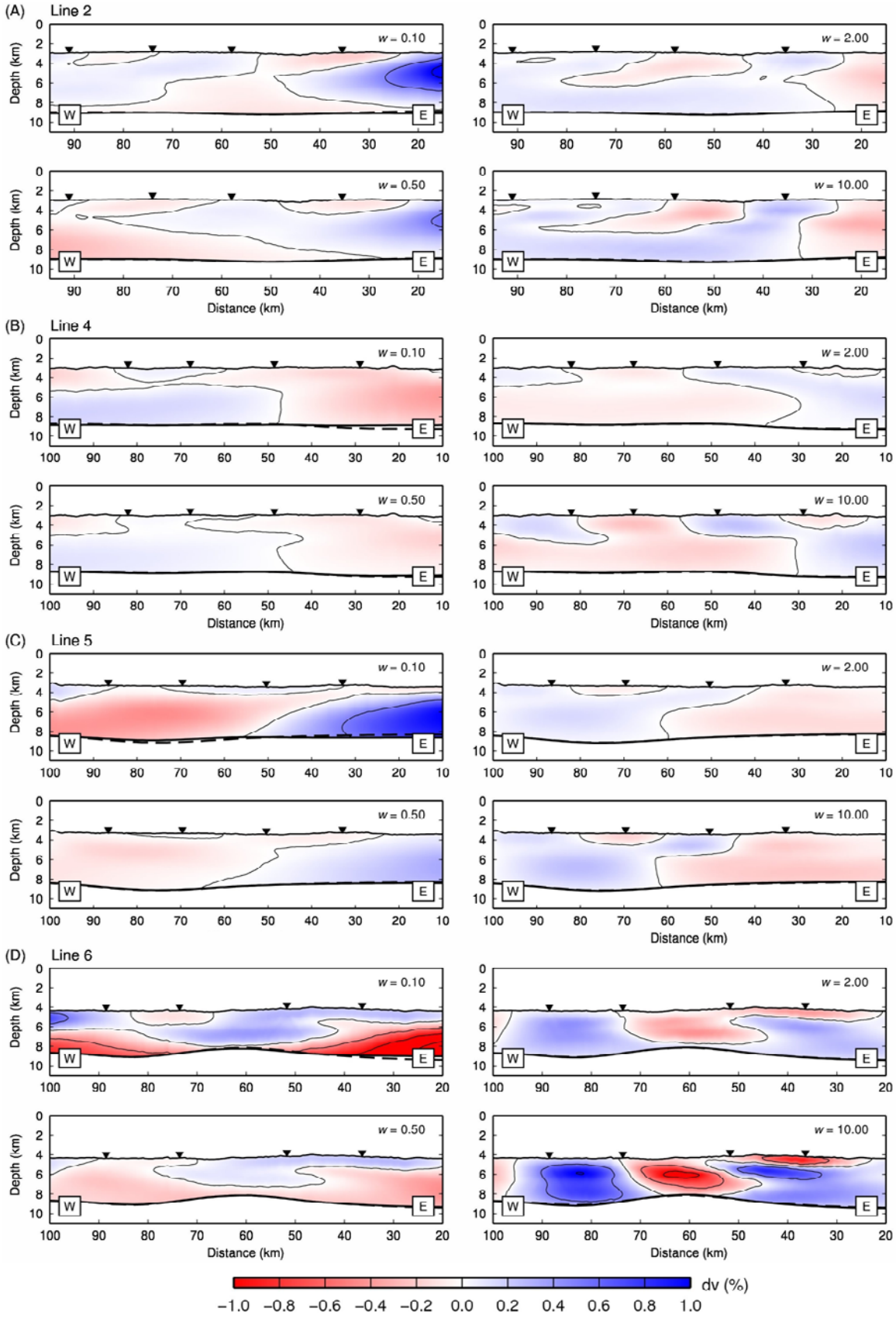
(A) Line 2
(B) Line 4
(C) Line 5
(D) Line 6
w = 0.10
w = 2.00
w = 0.50
w = 10.00
Depth (km)
Distance (km)
W
E
dv (%)
−1.0 −0.8 −0.6 −0.4 −0.2 0.0 0.2 0.4 0.6 0.8 1.0

Figure A2

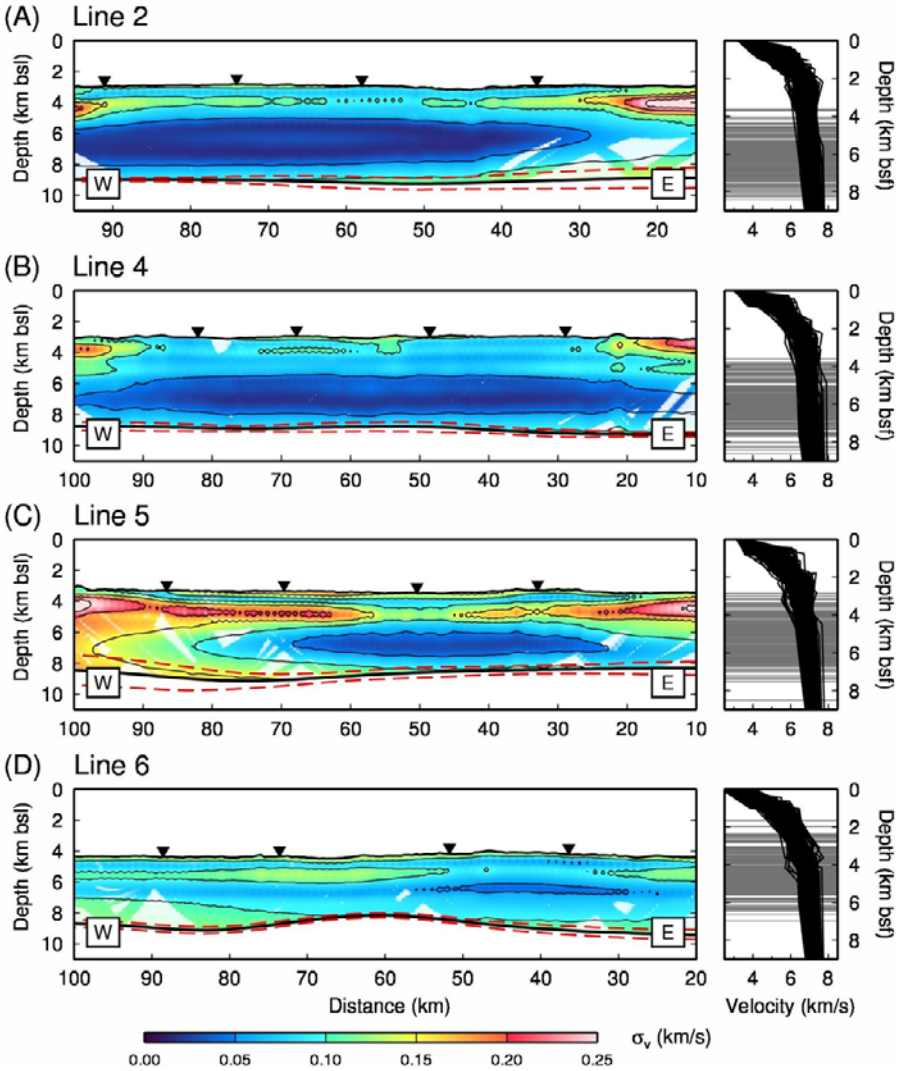

Figure A3. Monte Carlo uncertainty analysis. (a–d) The ensemble-averaged parameter uncertainty (standard deviation) for lines 2, 4, 5, and 6 using only those realizations with a data misfit of of $\chi 2 \leq 1.5$. Areas with no ray coverage are masked using the DWS. The contour interval is 0.05 km/s. Red dashed lines plot the 95% confidence intervals for the Moho reflector. On the right is depicted the 200 1-D random velocity models (black) and random starting reflector depths (gray) generated for the Monte Carlo series of inversions.

and velocity structure of no more than 0.2 km and ±0.5%, respectively.

A3. Monte Carlo Uncertainty Analysis

[40] We estimated the accuracy of our velocity models using a nonlinear Monte Carlo methodology. The posterior marginal probability density function (σ_M) describes the complete solution to the inverse problem and can be approximated through Bayesian inference by the distribution of many randomly sampled model realizations [*Sambridge and Mosegaard*, 2002; *Tarantola*, 2005]. We therefore determined individual parameter uncertainties using the sample variance of a solution ensemble constructed by inverting 200 random starting models (see Figure A3) together with the real traveltime data perturbed by random errors [*Matarese and Rodi*, 1994; *Tarantola*, 2005].

[41] A broad suite of starting models was created by adding zero-mean Gaussian perturbations in both velocity and depth to the median-averaged 1-D final solution for each refraction line. Velocities were varied by ±0.2 km/s and ±0.75 km/s at the base of layer 2A and at the layer 2/3 boundary, respectively. A perturbation of ±0.5 km/s was applied at the crust-mantle boundary (Moho) and ±0.2 km/s was used at the base of the model. Depth randomizations of ±0.5 km, ±0.825 km,

and ±1.35 km were introduced at the base of layer 2a, layer 2, and layer 3. The starting reflector depth, defined by the median-average crustal thickness for each refraction line, was independently varied by ±2.0 km.

[42] Rather than adding random white noise to the traveltime picks, we followed the method of *Zhang and Toksöz* [1998] and applied Gaussian-distributed $N(0, \sigma_1)$ common receiver errors and $N(0, \sigma_2)$ traveltime move-out errors to the data. We chose $\sigma_1 = 15$ ms to match the uncertainty of short-offset picks and substituted the RMS misfit of the data gradient in the preferred models for σ_2. The mean and maximum error magnitudes generated by this method were 43 ms and 158 ms for line 2, 40 ms and 165 ms for line 4, 44 ms and 174 ms for line 5, and 40 ms and 173 ms for line 6. All Monte Carlo inversions used the same parameterization, regularization, and top-down method as described for the preferred final solutions. Results with a data misfit of $\chi 2 > 1.5$ were discarded, reducing the realization count for each ensemble to 177 for line 2, 197 for line 4, 191 for line 5, and 124 for line 6. Since the variance of these ensembles is greater than would be found using the target misfit for the preferred final solutions ($\chi 2 \leq 1.0$), we consider the standard deviations in Figure A3 to represent upper bounds for the true parameter uncertainties.

[43] Figure A3 shows the results of the Monte Carlo procedure for lines 2, 4, 5, and 6. The $\pm 2\sigma$ confidence intervals plotted in Figure 8 are the 1-D median average σ-depth profiles derived from these surfaces. Standard deviations presented in this analysis essentially describe uncertainties associated with vertical variations in velocity. The 1.5-D geometry of the starting models, defined by the lateral expansion of the 1-D velocity profiles, precludes testing the resolution of horizontal variations. The largest uncertainties (0.15–0.25 km/s) generally appear in the high-gradient upper crustal region of the models where the discrete model parameterization can cause large changes in internodal velocities with small changes in velocity gradient. Increased uncertainty toward model edges likely reflects the lower ray density and unidirectional ray coverage in those areas. The velocity-depth trade-off results in elevated uncertainty values (0.10–0.15 km/s) near the Moho reflector, particularly in the region of line 5 west of 60 km previously identified in section 10.2. When ray coverage is dense, the standard deviation for the depth of the Moho falls below 0.2 km for all lines, while peak depth uncertainties are 0.3, 0.2, 0.5, and 0.2 for lines 2, 4, 5, and 6, respectively.

Acknowledgments

[44] We thank the captain, crew, and scientific staff of R/V *Maurice Ewing* cruise EW0114 for their ardent efforts under very difficult conditions. Personal thanks to Spahr Webb for many beneficial discussions and sound advice. We thank J. P. Canales, T. Minshull, and V. Salters for their helpful and insightful comments. The following software was used for data analysis and manuscript preparation: tomo2D [*Korenaga et al.*, 2000], MATLAB®7, GMT 4.2.1 [*Wessel and Smith*, 1998], and the Upicker package of MATLAB scripts maintained by W. Wilcock and the University of Washington Marine Geology and Geophysics research group. This work was supported by National Science Foundation grant OCE 99–11720. Partial funding was also provided by the Society of Exploration Geophysicists through the Anadarko/SEG Scholarship and the SEG Foundation General Scholarship. This is Lamont-Doherty Earth Observatory contribution 7209.

References

Baran, J. M., J. R. Cochran, S. M. Carbotte, and M. R. Nedimovic (2005), Variations in upper crustal structure due to variable mantle temperature along the Southeast Indian Ridge, *Geochem. Geophys. Geosyst.*, *6*, Q11002, doi:10.1029/2005GC000943.

Barry, K. M., D. A. Cavers, and C. W. Kneale (1975), Report on recommended standards for digital tape formats, *Geophysics*, *40*(2), 344–352, doi:10.1190/1.1440530.

Blacic, T. M., G. Ito, J. P. Canales, R. S. Detrick, and J. Sinton (2004), Constructing the crust along the Galapagos Spreading Center 91.3°–95.5°W: Correlation of seismic layer 2A with axial magma lens and topographic characteristics, *J. Geophys. Res.*, *109*, B10310, doi:10.1029/2004JB003066.

Bown, J. W., and R. S. White (1994), Variation with spreading rate of oceanic crustal thickness and geochemistry, *Earth Planet. Sci. Lett.*, *121*(3–4), 435–449, doi:10.1016/0012-821X(94)90082-5.

Buck, W. R., S. M. Carbotte, and C. Mutter (1997), Controls on extrusion at mid-ocean ridges, *Geology*, *25*, 935–938, doi:10.1130/0091-7613(1997)025<0935:COEAMO>2.3.CO;2.

Canales, J. P., R. S. Detrick, J. Lin, J. A. Collins, and D. R. Toomey (2000), Crustal and upper mantle seismic structure beneath the rift mountains and across a nontransform offset at the Mid-Atlantic Ridge (35°N), *J. Geophys. Res.*, *105*(B2), 2699–2720, doi:10.1029/1999JB900379.

Canales, J. P., G. Ito, R. S. Detrick, and J. M. Sinton (2002), Crustal thickness along the western Galápagos Spreading Center and the compensation of the Galápagos hotspot swell, *Earth Planet. Sci. Lett.*, *203*(1), 311–327, doi:10.1016/S0012-821X(02)00843-9.

Canales, J. P., R. S. Detrick, S. M. Carbotte, G. M. Kent, J. B. Diebold, A. Harding, J. Babcock, M. R. Nedimović, and E. van Ark (2005), Upper crustal structure and axial topography at intermediate spreading ridges: Seismic constraints from the southern Juan de Fuca Ridge, *J. Geophys. Res.*, *110*, B12104, doi:10.1029/2005JB003630.

Cande, S. C., and J. C. Mutter (1982), A revised identification of the oldest sea-floor spreading anomalies between Austra-

lia and Antarctica, *Earth Planet Sci. Lett.*, *140*(2), 151–160, doi:10.1016/0012-821X(82)90190-X.

Carbotte, S. M., C. Mutter, J. C. Mutter, and G. Ponce-Correa (1998), Influence of magma supply and spreading rate on crustal magma bodies and emplacement of the extrusive layer: Insights from the East Pacific Rise at lat 16°N, *Geology*, *26*(5), 455–458, doi:10.1130/0091-7613(1998)026<0455:IOMSAS>2.3.CO;2.

Chen, Y. J. (1992), Oceanic crustal thickness verses spreading rate, *Geophys. Res. Lett.*, *19*(8), 753–756, doi:10.1029/92GL00161.

Chen, Y. J. (1996), Constraints on melt production rate beneath the mid-ocean ridges based on passive flow models, *Pure Appl. Geophys.*, *146*(3–4), 589–620, doi:10.1007/BF00874735.

Chen, Y. J., and W. J. Morgan (1990a), Rift valley/no rift valley transition at mid-ocean ridges, *J. Geophys. Res.*, *95*(B11), 17,571–17,581, doi:10.1029/JB095iB11p17571.

Chen, Y. J., and W. J. Morgan (1990b), A nonlinear rheology model for mid-ocean ridge axis topography, *J. Geophys. Res.*, *95*(B11), 17,583–17,604, doi:10.1029/JB095iB11p17583.

Christensen, N. I., and J. D. Smewing (1981), Geology and seismic structure of the northern section of the Oman ophiolite, *J. Geophys. Res.*, *86*(B4), 2545–2555, doi:10.1029/JB086iB04p02545.

Cochran, J. R., and M. Talwani (1977), Free-air gravity anomalies in the world's oceans and their relationship to residual elevation, *Geophys. J. Int.*, *50*(3), 495–552, doi:10.1111/j.1365-246X.1977.tb01334.x.

Cochran, J., J.-C. Sempéré, and S. Team (1997), The Southeast Indian Ridge between 88°E and 118°E: Gravity anomalies and crustal accretion at intermediate spreading rates, *J. Geophys. Res.*, *102*(B7), 15,463–15,487, doi:10.1029/97JB00511.

Conder, J. A., D. S. Scheirer, and D. W. Forsyth (2000), Seafloor spreading on the Amsterdam-St. Paul hotspot plateau, *J. Geophys. Res.*, *105*(B4), 8263–8277, doi:10.1029/1999JB900406.

Constable, S. C., R. L. Parker, and C. G. Constable (1987), Occam's inversion: A practical algorithm for generating smooth models from electromagnetic sounding data, *Geophysics*, *52*(3), 289–300, doi:10.1190/1.1442303.

DeMets, C., R. G. Gordon, D. F. Argus, and S. Stein (1994), Effect of recent revisions to the geomagnetic reversal time scale on estimates of current plate motions, *Geophys. Res. Lett.*, *21*(20), 2191–2194, doi:10.1029/94GL02118.

Detrick, R., J. Collins, R. Stephen, and S. Swift (1994), In situ evidence for the nature of the seismic layer 2/3 boundary in oceanic crust, *Nature*, *370*(6487), 288–290, doi:10.1038/370288a0.

Dijkstra, E. W. (1959), A note on two problems in connexion with graphs, *Numer. Math.*, *1*, 269–271, doi:10.1007/BF01386390.

Forsyth, D. W., R. L. Ehrenbard, and S. Chapin (1987), Anomalous upper mantle beneath the Australian-Antarctic Discordance, *Earth Planet. Sci. Lett.*, *84*(4), 471–478, doi:10.1016/0012-821X(87)90011-2.

Géli, L., J. R. Cochran, T. C. Lee, J. Francheteau, C. Labails, C. Fouchet, and D. Christie (2007), Thermal regime of the Southeast Indian Ridge between 88°E and 140°E: Remarks on the subsidence of the ridge flanks, *J. Geophys. Res.*, *112*, B10101, doi:10.1029/2006JB004578.

Goff, J. A., Y. Ma, A. Shah, J. R. Cochran, and J.-C. Sempéré (1997), Stochastic analysis of seafloor morphology on the flank of the Southeast Indian Ridge: The influence of ridge morphology on the formation of abyssal hills, *J. Geophys. Res.*, *102*(B7), 15,521–15,534, doi:10.1029/97JB00781.

Gurnis, M., and R. D. Müller (2003), The origin of the Australian-Antarctic Discordance from an ancient slab and mantle wedge, in *The Evolution and Dynamics of the Australian Plate*, edited by R. R. Hillis and R. D. Muller, *Geol. Soc. Am. Spec. Pap.*, *372*, 422–423.

Gurnis, M., R. D. Müller, and L. Moresi (1998), Cretaceous vertical motion of Australia and the Australian Antarctic Discordance, *Science*, *279*(5356), 1499–1504, doi:10.1126/science.279.5356.1499.

Hamelin, B., B. Dupré, and C. J. Allègre (1986), Pb-Sr-Nd isotopic data of Indian Ocean ridges: New evidence of large-scale mapping of mantle heterogeneities, *Earth Planet. Sci. Lett.*, *76*(3–4), 288–298, doi:10.1016/0012-821X(86)90080-4.

Hayes, D. (1988), Age-depth relationships and depth anomalies in the Southeast Indian Ocean and South Atlantic Ocean, *J. Geophys. Res.*, *93*(B4), 2937–2954, doi:10.1029/JB093iB04p02937.

Heezen, B. C. (1960), The rift in the ocean floor, *Sci. Am.*, *203*(4), 98–110.

Hopson, C. A., R. G. Coleman, R. T. Gregory, J. S. Pallister, and E. H. Bailey (1981), Geologic section through the Samail ophiolite and associated rocks along a Muscat-Ibra Transect, southeastern Oman Mountains, *J. Geophys. Res.*, *86*(B4), 2527–2544, doi:10.1029/JB086iB04p02527.

Houtz, R. E., J. Ewing, and P. Buhl (1970), Seismic data from sonobuoy stations in the northern and equatorial Pacific, *J. Geophys. Res.*, *75*(26), 5093–5111, doi:10.1029/JB075i026p05093.

Jokat, W., and M. C. Schmidt-Aursch (2007), Geophysical characteristics of the ultraslow spreading Gakkel Ridge, Artic Ocean, *Geophys. J. Int.*, *168*(3), 983–998, doi:10.1111/j.1365-246X.2006.03278.x.

Kane, K. A., and D. E. Hayes (1994), A new relationship between subsidence rate and zero-age depth, *J. Geophys. Res.*, *99*(B11), 21,759–21,777, doi:10.1029/94JB01747.

Klein, E. M., and C. H. Langmuir (1987), Global correlations of ocean ridge basalt chemistry with axial depth and crustal thickness, *J. Geophys. Res.*, *92*(B8), 8089–8115, doi:10.1029/JB092iB08p08089.

Klein, E. M., C. H. Langmuir, A. Zindler, H. Staudigel, and B. Hamelin (1988), Isotope evidence of a mantle convection boundary at the Australian-Antarctic Discordance, *Nature*, *333*(6174), 623–629, doi:10.1038/333623a0.

Klein, E. M., C. H. Langmuir, and H. Staudigel (1991), Geochemistry of basalts from the Southeast Indian Ridge, 115°E–138°E, *J. Geophys. Res.*, *96*(B2), 2089–2107, doi:10.1029/90JB01384.

Korenaga, J., W. S. Holbrook, G. M. Kent, P. B. Kelemen, R. S. Detrick, H.-C. Larsen, J. R. Hopper, and T. Dahl-Jensen (2000), Crustal structure of the southeast Greenland margin from joint refraction and reflection seismic tomography, *J. Geophys. Res.*, *105*(B9), 21,591–21,614, doi:10.1029/2000JB900188.

Kuo, B.-Y., C.-H. Chen, and Y.-S. Zhang (1996), A fast velocity anomaly to the west of the Australian- Antarctic Discordance, *Geophys. Res. Lett.*, *23*(17), 2239–2242, doi:10.1029/96GL02144.

Lin, J., and J. Phipps Morgan (1992), The spreading rate dependence of three-dimensional mid-ocean ridge gravity structure, *Geophys. Res. Lett.*, *19*(1), 13–16, doi:10.1029/91GL03041.

Lines, L. (1993), Ambiguity in analysis of velocity and depth, *Geophysics*, *58*(4), 596–597, doi:10.1190/1.1443443.

Ma, Y., and J. Cochran (1996), Transitions in axial morphology along the Southeast Indian Ridge, *J. Geophys. Res.*, *101*(B7), 15,849–15,866, doi:10.1029/95JB03038.

Ma, Y., and J. Cochran (1997), Bathymetric roughness of the Southeast Indian Ridge: Implications for crustal accretion at intermediate spreading rate mid-ocean ridges, *J. Geophys. Res.*, *102*(B8), 17,697–17,711, doi:10.1029/97JB01280.

Macdonald, K. C. (1982), Mid-ocean ridges: Fine scale tectonic, volcanic and hydrothermal processes within the plate boundary zone, *Annu. Rev. Earth Planet. Sci.*, *10*(1), 155–190, doi:10.1146/annurev.ea.10.050182.001103.

Macdonald, K. C. (1986), The crest of the Mid-Atlantic Ridge: Models for crustal generation processes and tectonics, in *The Geology of North America*, vol. M, *The Western North Atlantic Region*, edited by P. R. Vogt and B. E. Tucholke, pp. 51–68, Geol. Soc. of Am., Boulder, Colo.

Macdonald, K. C. (1989), Tectonic and magmatic processes on the East Pacific Rise, in *The Geology of North America*, vol. N, *The Eastern Pacific Ocean and Hawaii*, edited by E. L. Winter, D. M. Hussong, and R. W. Decker, pp. 93–110, Geol. Soc. of Am., Boulder, Colo.

Mahoney, J. J., D. W. Graham, D. M. Christie, K. T. M. Johnson, L. S. Hall, and D. L. Vonderhaar (2002), Between a hotspot and a cold spot; isotopic variation in the Southeast Indian Ridge asthenosphere, 86°E–118°E, *J. Petrol.*, *43*(7), 1155–1176, doi:10.1093/petrology/43.7.1155.

Malinverno, A. (1993), Transition between a valley and a high at the axis of mid-ocean ridges, *Geology*, *21*(7), 639–642, doi:10.1130/0091-7613(1993)021<0639:TBAVAA>2.3.CO;2.

Matarese, J. R., and W. L. Rodi (1994), Monte Carlo uncertainty measures in nonlinear traveltime tomography, *SEG Expanded Abstr.*, *13*(1), 984–987, doi:10.1190/1.1932060.

McKenzie, D. (1984), The generation and compaction of partially molten rock, *J. Petrol.*, *25*(3), 713–765.

Menard, H. W. (1960), The East Pacific Rise, *Science*, *132*(3441), 1737–1746, doi:10.1126/science.132.3441.1737.

Menard, H. W. (1967), Sea floor spreading, topography, and the second layer, *Science*, *157*(3791), 923–924, doi:10.1126/science.157.3791.923.

Michard, A., R. Montigny, and R. Schlich (1986), Geochemistry of the mantle beneath the Rodriguez Triple Junction and the South-East Indian Ridge, *Earth Planet. Sci. Lett.*, *78*(1), 104–114, doi:10.1016/0012-821X(86)90176-7.

Minshull, T. A., N. J. Bruguier, and J. M. Brozena (2003), Seismic structure of the Mid-Atlantic Ridge, 8–9°S, *J. Geophys. Res.*, *108*(B11), 2513, doi:10.1029/2002JB002360.

Minshull, T. A., M. R. Muller, and R. S. White (2006), Crustal structure of the Southwest Indian Ridge at 66°S: Seismic constraints, *Geophys. J. Int.*, *166*(1), 135–147, doi:10.1111/j.1365-246X.2006.03001.x.

Moser, T. J. (1991), Shortest path calculation of seismic rays, *Geophysics*, *56*(1), 59–67, doi:10.1190/1.1442958.

Moser, T. J., G. Nolet, and R. Snieder (1992), Ray bending revisited, *Bull. Seismol. Soc. Am.*, *82*(1), 259–288.

Murase, T., and A. R. McBirney (1973), Properties of some common igneous rocks and their melts at high temperatures, *Geol. Soc. Am. Bull.*, *84*(11), 3563–3592, doi:10.1130/0016-7606(1973)84<3563:POSCIR>2.0.CO;2.

Mutter, C. Z., and J. C. Mutter (1993), Variations in thickness of layer 3 dominate oceanic crustal structure, *Earth Planet. Sci. Lett.*, *117*(1–2), 295–317, doi:10.1016/0012-821X(93)90134-U.

Paige, C. C., and M. A. Saunders (1982), LSQR: An algorithm for sparse linear equations and sparse least squares, *ACM Trans. Math. Software*, *8*(1), 43–71, doi:10.1145/355984.355989.

Peal, K. R., G. M. Purdy, D. E. Koelsch, and F. B. Wooding (1993), A simple ocean bottom hydrophone with 200 Megabyte data capacity, *Tech. Rep. WHOI-93–31*, Woods Hole Oceanogr. Inst., Woods Hole, Mass.

Phillips, W. S., and M. C. Fehler (1991), Traveltime tomography: A comparison of popular methods, *Geophysics*, *56*(10), 1639–1649, doi:10.1190/1.1442974.

Phipps Morgan, J., and Y. J. Chen (1993a), Dependence of ridge-axis morphology on magma supply and spreading rate, *Nature*, *364*(6439), 706–708, doi:10.1038/364706a0.

Phipps Morgan, J., and Y. J. Chen (1993b), The genesis of oceanic crust: Magma injection, hydrothermal circulation, and crustal flow, *J. Geophys. Res.*, *98*(B4), 6283–6297, doi:10.1029/92JB02650.

Phipps Morgan, J., and D. T. Sandwell (1994), Systematics of ridge propagation south of 30°S, *Earth Planet. Sci. Lett.*, *121*(1–2), 245–258, doi:10.1016/0012-821X(94)90043-4.

Purdy, G. M., L. S. L. Kong, G. L. Christeson, and S. C. Solomon (1992), Relationship between spreading rate and the seismic structure of mid-ocean ridges, *Nature*, *355*(6363), 815–817, doi:10.1038/355815a0.

Pyle, D. G., D. M. Christie, and J. J. Mahoney (1992), Resolving an isotopic boundary within the Australian-Antarctic discordance, *Earth Planet. Sci. Lett.*, *112*(1–4), 161–178, doi:10.1016/0012-821X(92)90014-M.

Raitt, R. W. (1963), The crustal rocks, in *The Sea*, vol. 3, edited by M. N. Hill, pp. 85–102, Wiley-Interscience, New York.

Rawlinson, N., and M. Sambridge (2003), Seismic traveltime tomography of the crust and lithosphere, *Adv. Geophys.*, *46*, 181–198.

Ritzwoller, M. H., N. M. Shapiro, and G. M. Leahy (2003), A resolved mantle anomaly as the cause of the Australian-Antarctic Discordance, *J. Geophys. Res.*, *108*(B12), 2559, doi:10.1029/2003JB002522.

Ross, W. S. (1994), The velocity-depth ambiguity in seismic traveltime data, *Geophysics*, *59*(5), 830–843, doi:10.1190/1.1443641.

Royer, J.-Y., and D. T. Sandwell (1989), Evolution of the eastern Indian Ocean since the Late Cretaceous: Constraints from Geosat altimetry, *J. Geophys. Res.*, *94*(B10), 13,755–13,782, doi:10.1029/JB094iB10p13755.

Sambridge, M., and K. Mosegaard (2002), Monte Carlo methods in geophysical inverse problems, *Rev. Geophys.*, *40*(3), 1009, doi:10.1029/2000RG000089.

Sandwell, D. T., and W. H. F. Smith (1997), Marine gravity anomaly from Geosat and ERS 1 satellite altimetry, *J. Geophys. Res.*, *102*(B5), 10,039–10,054, doi:10.1029/96JB03223.

Scheirer, D. S., D. W. Forsyth, J. A. Conder, M. A. Eberle, S.-H. Hung, K. T. M. Johnson, and D. W. Graham (2000), Anomalous seafloor spreading of the Southeast Indian Ridge near the Amsterdam-St. Paul Plateau, *J. Geophys. Res.*, *105*(B4), 8243–8262, doi:10.1029/1999JB900407.

Sempéré, J.-C., J. R. Cochran, and the SEIR Scientific Team (1997), The Southeast Indian Ridge between 88°E and 118°E: Variations in crustal accretion at constant spreading rate, *J. Geophys. Res.*, *102*(B7), 15,489–15,505, doi:10.1029/97JB00171.

Shah, A., and J.-C. Sempéré (1998), Morphology of the transition from an axial high to a rift valley at the Southeast Indian Ridge and the relation to variations in mantle temperature, *J. Geophys. Res.*, *103*(B3), 5203–5223, doi:10.1029/97JB03110.

Sinton, J., R. Detrick, J. P. Canales, G. Ito, and M. Behn (2003), Morphology and segmentation of the western Galápagos Spreading Center, 90.5°–98°W: Plume-ridge interaction at an intermediate spreading ridge, *Geochem. Geophys. Geosyst.*, *4*(12), 8515, doi:10.1029/2003GC000609.

Small, C. (1994), A global analysis of mid-ocean ridge axial topography, *Geophys. J. Int.*, *116*(1), 64–84, doi:10.1111/j.1365-246X.1994.tb02128.x.

Small, C. (1995), Observations of ridge-hotspot interactions in the Southern Ocean, *J. Geophys. Res.*, *100*(B9), 17,931–17,946, doi:10.1029/95JB01377.

Small, C. (1998), Global systematics of mid-ocean ridge morphology, in *Faulting and Magmatism at Mid-Ocean Ridges*, *Geophys. Monogr. Ser.*, vol. 106, edited by W. R. Buck et al., pp. 1–25, AGU, Washington, D.C.

Small, C., and D. T. Sandwell (1989), An abrupt change in ridge axis gravity with spreading rate, *J. Geophys. Res.*, *94*(B12), 17,383–17,392, doi:10.1029/JB094iB12p17383.

Small, C., and D. T. Sandwell (1992), An analysis of ridge axis gravity roughness and spreading rate, *J. Geophys. Res.*, *97*(B3), 3235–3245, doi:10.1029/91JB02465.

Talwani, M., C. C. Windisch, and M. G. Langseth Jr. (1971), Reykjanes ridge crest: A detailed geophysical study, *J. Geophys. Res.*, *76*(2), 473–517, doi:10.1029/JB076i002p00473.

Tarantola, A. (2005), *Inverse Problem Theory and Methods for Model Parameter Estimation*, 342 pp., SIAM, Philadelphia, Pa.

Tikku, A. A., and S. C. Cande (1999), The oldest magnetic anomalies in the Australian-Antarctic Basin: Are they isochrons?, *J. Geophys. Res.*, *104*(B1), 661–678, doi:10.1029/1998JB900034.

Tolstoy, M., A. J. Harding, and J. A. Orcutt (1993), Crustal thickness on the Mid-Atlantic Ridge: Bull's-eye gravity anomalies and focused accretion, *Science*, *262*(5134), 726–729, doi:10.1126/science.262.5134.726.

Tolstoy, M., J. R. Cochran, S. M. Carbotte, and J. S. Floyd (2002), Crustal Thickness on the South East Indian Ridge from OBH Data, *Eos Trans. AGU*, *83*(47), Fall Meet. Suppl., Abstract T12B–1314.

van Avendonk, H. J. A., A. J. Harding, J. A. Orcutt, and J. S. McClain (1998), A two-dimensional tomographic study of the Clipperton transform fault, *J. Geophys. Res.*, *103*(B8), 17,885–17,900, doi:10.1029/98JB00904.

van Avendonk, H. J. A., D. J. Shillington, W. S. Holbrook, and M. J. Hornbach (2004), Inferring crustal structure in the Aleutian island arc from a sparse wide-angle seismic data set, *Geochem. Geophys. Geosyst.*, *5*, Q08008, doi:10.1029/2003GC000664.

Veevers, J. J. (1986), Breakup of Australia and Antarctica estimated as mid-Cretaceous (95 ± 5 Ma) from magnetic and seismic data at the continental margin, *Earth Plant. Sci. Lett.*, *77*(1), 91–99, doi:10.1016/0012-821X(86)90135-4.

Vera, E. E., J. C. Mutter, P. Buhl, J. A. Orcutt, A. J. Harding, M. E. Kappus, R. S. Detrick, and T. M. Brocher (1990), The structure of 0- to 0.2-m.y.-old oceanic crust at 9°N on the East Pacific Rise from expanded spread profiles, *J. Geophys. Res.*, *95*(B10), 15,529–15,556, doi:10.1029/JB095iB10p15529.

Wang, X., and J. R. Cochran (1995), Along-axis gravity gradients at mid-ocean ridges: Implications for mantle flow and axial morphology, *Geology*, *23*(1), 29–32, doi:10.1130/0091-7613(1995)023<0029:AAGGAM>2.3.CO;2.

Weissel, J., and D. Hayes (1974), The Australian-Antarctic Discordance: New results and implications, *J. Geophys. Res.*, *79*(17), 2579–2587, doi:10.1029/JB079i017p02579.

Wessel, P., and W. H. F. Smith (1998), New, improved version of generic mapping tools released, *Eos Trans. AGU*, *79*(47), 579, doi:10.1029/98EO00426.

West, B. P., W. S. D. Wilcock, J.-C. Sempéré, and L. Géli (1997), Three-dimensional structure of asthenospheric flow beneath the Southeast Indian Ridge, *J. Geophys. Res.*, *102*(B4), 7783–7802, doi:10.1029/96JB03895.

White, R. S., D. McKenzie, and R. K. O'Nions (1992), Oceanic crustal thickness from seismic measurements and rare earth element inversions, *J. Geophys. Res.*, *97*(B13), 19,683–19,715, doi:10.1029/92JB01749.

Wilson, D. S., et al. (2006), Drilling to Gabbro in intact ocean crust, *Science*, *312*(5776), 1016–1020, doi:10.1126/science.1126090.

Zelt, C. A. (1999), Modelling strategies and model assessment for wide-angle seismic traveltime data, *Geophys. J. Int.*, *139*(1), 183–204, doi:10.1046/j.1365-246X.1999.00934.x.

Zelt, C. A., and D. A. Forsyth (1994), Modeling wide-angle seismic data for crustal structure: Southeastern Grenville Province, *J. Geophys. Res.*, *99*(B6), 11,687–11,704, doi:10.1029/93JB02764.

Zhang, J., and M. N. Toksöz (1998), Nonlinear refraction traveltime tomography, *Geophysics*, *63*(5), 1726–1737, doi:10.1190/1.1444468.